SACLANT UNDERSEA RESEARCH CENTRE REPORT

RESONANCE SCATTERING ANALYSIS BY AUTOREGRESSIVE MODELS APPLIED TO AIR-FILLED, CYLINDRICAL, THIN WALLED SHELLS IN WATER

A. Tesei, W. Fox, A. Maguer, A. Løvik

October 1997

19980522 065

DTIC QUALITY INSPECTED 4

NORTH ATLANTIC TREATY ORGANIZATION

Resonance scattering analysis by autoregressive models applied to air-filled, cylindrical, thin walled shells in water

A. Tesei, W. L. J. Fox, A. Maguer, and A. Løvik

The content of this document pertains to work performed under Project 031-2 of the SACLANTCEN Programme of Work. The document has been approved for release by The Director, SACLANTCEN.

Jan L. Spoelstra
Director

intentionally blank page

Resonance scattering analysis by autoregressive models applied to air-filled, cylindrical, thin walled shells in water

A. Tesei, W. L. J. Fox, A. Maguer, and A. Løvik

Executive Summary:

Current research on mine classification systems is concerned with using broadband sonar signals to insonify mine-like targets, and applying advanced signal processing techniques to the backscattered signals in order to analyze them in the time, frequency, and other domains.

One characteristic of target echoes which may provide classification clues is the so-called resonance scattering response, the characteristics of which are caused by the elastic properties of a given target. This report presents algorithms for extracting resonance information based on autoregressive (AR) spectral estimation techniques. AR modeling is a parametric approach to the analytical representation of the frequency response of linear systems. A target is assumed to be a linear acoustic system with a rational transfer function. The number and values of the AR parameters are correlated with the resonance frequencies proper of the target. The location of resonances in the frequency domain extracted from the backscattered time series is related to specific physical characteristics of the target. Here AR-based methods are applied to simulated and experimental data for air-filled, cylindrical, thin walled shells. The algorithms are shown to be successful in predicting parameters such as the outer radius, shell material, and shell thickness.

The analysis of acoustic scattering by objects with very simple shapes in the free field is a first step towards the characterization and classification of mine-like targets under more realistic operating conditions.

Future work will attempt to extend the algorithms to more general target classes including real mines.

intentionally blank page

Resonance scattering analysis by autoregressive models applied to air-filled, cylindrical, thin walled shells in water

A. Tesei, W.L.J. Fox, A. Maguer, and A. Løvik

Abstract:

Autoregressive (AR) parametric spectral estimation of the scatterer transfer function is applied to the analysis of acoustic scattering by elastic objects.

In accordance with Resonance Scattering Theory (RST), the specular and resonance components of the scattering field are differentiated. AR models and consequent resonance analysis are applied to both the global scattering response and to the resonance component separately.

The AR-based representation is useful for detecting and localizing resonances in the frequency domain. The capability of AR models to estimate resonance frequencies accurately is shown. Among the extracted poles of the AR model, a subset of resonance frequencies is selected and processed in order to characterize a scattering object in terms of geometrical and geophysical parameters on the basis of analytical matching relations, derived from the RST.

The targets considered are elastic, cylindrical, thin walled shells in water under free-field conditions. Analysis is performed on simulated and real data in the ka range $(0,50]$.

Keywords: Free-field acoustic scattering, resonance analysis, AR-based spectral estimation.

Contents

intentionally blank page

1

Introduction

This report is in the field of direct and inverse acoustic scattering problems applied to submerged elastic objects. Attention is focused on scattering resonance analysis, where the final aims are geometrical/physical parameter estimation and object classification.

The analysis presented here concerns acoustic scattering at low-intermediate frequencies by elastic man-made objects submerged in the sea water under free-field conditions. Limiting the analysis to low-intermediate frequency ranges ($ka \in (0,50]$) means that we can isolate relatively few families of resonance waves and focus investigation and processing on their extraction, identification and interpretation.

The present investigation is limited to fluid-loaded, air-filled, circular cylindrical shells insonified at broadside aspect (by aspect angle we mean the angle between the direction of incidence and the cylinder axis). If the shells were evacuated instead of air-filled, scattering behavior would be unaffected.

The analysis starts from basic theoretical considerations derived from Resonance Scattering Theory (RST) [1][2], under the conditions of *far-field backscattering by infinite circular cylindrical targets excited by plane waves at normal incidence* (Fig. 1.1).
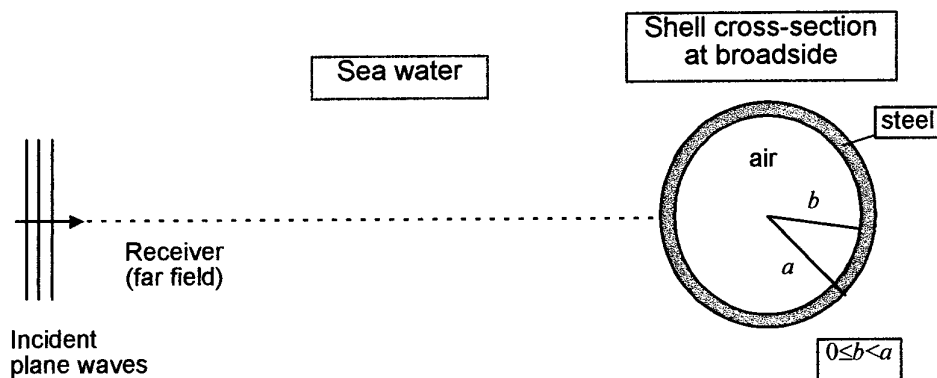

Fig. 1.1. Geometry of the problem: scattering from an elastic cylinder at broadside.

In the case study proposed here, the target has finite length [3], nevertheless RST is shown to provide a valuable reference for basic investigation and data interpretation, and is used to build matching models the validation of which using real data achieved good results.

The constraints that must be satisfied (at least approximately) for maintaining the validity of the selected theoretical considerations are the hypotheses concerning the observation point (in the far-field of the target), incidence angle (normal) and shell inner medium (vacuum or air).

According to RST the frequency response of a scattering system can be divided into:

- a non-resonant *background* component (consisting of the specular echo and fluid-born creeping waves around the target cross-section) which is aspect-dependent, and
- a *resonance* component, containing both aspect-dependent and aspect-independent frequency components (deriving from the generation of peripheral waves of many types).

Among the resonances generated by the peripheral waves one can distinguish [2]:

- a set of resonances coinciding with the natural eigen-frequencies of the target, which can be useful features for target classification purposes as they are *aspect-independent*, and
- a set of resonances (e.g., the Lamb-type and Scholte-Stoneley waves) the presence and/or location of which in frequency are *aspect-dependent*, and which can be useful features mainly for determining target orientation, or for estimating other geometrical and geophysical target properties when the aspect angle is known *a priori*.

As the present work is performed under the hypothesis of normal incidence, the aspect dependence of the selected resonance families will not be examined. The results obtained in [2][4], however, suggest that most of the resonance scattering features to be examined in this work are aspect-dependent. Future work will involve analysis of scattering by targets at various aspect angles.

On the basis of RST, many processing methods have been developed (e.g., [5][6][7][8]) for separating the resonance from the background components. In this work, the Azimi-Sadjadi algorithm is employed, which uses an adaptive filtering process based on "Recursive Least Squares learning" [7]. De Billy in [5] showed how the contribution of certain families of resonances changes in the scattered wave-field spectrum as either the global response or only the pure resonant components are taken into account. Hence, he analyzed separately and then compared the global and the pure resonance responses by applying gates at various time instants. In particular, he analyzed the *global response* (including the specular echo), and the responses obtained by applying one time gate immediately after the end of the specular echo (hence obtaining the *pure resonance component*) and one so distant from the end of the specular echo, that the resonance component do not include any reflection from the target shape (hence providing the so-called *far resonance component*). In this work these three components are also analyzed.

In Section 2 a set of wave families generated by scattering are selected and interpreted by means of RST. They are considered as significant features for estimating target properties and, hence, discriminating between different targets. Their peculiarities are presented and discussed. Resonance features are selected on the basis of simulated data, which are represented and analyzed in the frequency domain. The simulation method [3] is based on the solution of a 2D scattering problem according to RST; as a consequence, it assumes all the simplifying conditions mentioned above to be complied with.

This investigation indicates which geometrical or mechanical target parameters can be correlated with these physical scattering phenomena, and how to build related analytical matching models. From the physical interpretation of the generated waves, analytical relations can be deduced linking resonance properties with some parameters of interest (e.g., target dimensions, materials, etc.). Most of the analytical models proposed in Section 2 start from resonance frequency identification and localization. They allow estimation of the outer radius, some properties of the material and the shell thickness of the scattering target, given its shape.

Most of the developed matching models require the accurate estimate of a set of resonance frequencies as an input. To this end, autoregressive (AR) modeling of the scattered response by an elastic object is applied. From the poles estimated by the parametric model, a set of resonance frequencies can be selected. AR-based parametric methods of spectrum estimation and their capabilities are briefly outlined in Section 3

The proposed methods of resonance extraction and processing were validated using simulated data and real data scattered by air-filled elastic circular cylindrical shells in sea water, insonified at broadside by broadband pulses. The analysis was performed separately on the global, pure and far resonance components of the scattered response. Results are given and discussed in Section 4.

Conclusions on the advantages and limitations of the developed methods are provided in Section 5, where future work is also outlined.

2

Resonance scattering theory

This investigation is derived from RST and, in particular, from the analysis of simulated data [1][2][3] assuming far-field backscattering from an infinitely long elastic circular cylindrical shell insonified in the free-field by plane acoustic waves at broadside.

The mathematical approach is based on the normal mode series formulation, consisting of the decomposition of the backscattered pressure field into an infinite summation of modal components which depend on both the mechanical properties and the geometry of the scatterer. The general form of the far-field backscattered pressure field at normal incidence can be expressed as [2]

$$p_s \approx p_* e^{j(kr-\omega t)} \left(\frac{a}{2r}\right)^{1/2} \sum_{n=0}^{\infty} \varepsilon_n (j\pi ka)^{-1/2} \frac{D_n^1(\omega)}{D_n(\omega)} \tag{2.1}$$

where ω is the angular frequency, k is the wave number with respect to the outer medium, r is the range, a is the cylinder outer radius, ε_n is the Neumann factor ($\varepsilon_0 = 1$, $\varepsilon_n = 2$ for $n>0$), and p_* is the amplitude of the incident plane wave $p_i = p_* e^{j(kr-\omega t)}$.

$D_n^1(\omega)$ and $D_n(\omega)$ are determinants computed from the boundary conditions of the problem (i.e., continuity of stress and displacement at both interfaces). For this reason they depend on all the mechanical and geometrical parameters listed in Table 2.1. The scatterer Transfer Function (TF), $H(\cdot)$, is defined as the ratio between the scattered pressure p_s and the incident wave p_i.

Shell Parameters	Inner material Parameters (Fluid)	Outer Medium Parameters (Fluid)
outer radius: a inner radius: b relative thickness: $h = d/a$; $d = a - b$; $0<h\leq1$ density: ρ_1 compressional speed: c_p shear speed: c_s	density: ρ_i sound speed: c_i	density: ρ sound speed: c

Table 2.1. Geometrical and mechanical parameters influencing acoustic backscattering.

The geometrical and mechanical parameters of the target and the physical properties of the inner and outer media are used as input for generating simulated data. Appendix A contains the physical parameters for a set of reference media. In the present work, the inner medium is air.

It is known [2] that the zeros of $D_n(\omega)$ correspond to shell resonance frequencies, and are connected to the propagation of circumferential acoustic waves of different types. Important features of these waves are their group and phase speed dispersion curves which describe how the group and phase speeds of a peripheral wave vary with frequency. They are related to the geometry and to the physical properties of the scatterer. The dispersion curves directly depend on the location of the generated resonances, as specified by some relationships to be presented in Section 2.2.1. Attention is focused on the *localization of resonances* of several kinds in the frequency domain.

In RST, each resonance frequency is labeled by the index pair (l,n), where l is used for distinguishing among different families of elastic circumferential waves characterized by their own phase and group speeds, and n refers to the modal order of vibration. In general, the value of the index l increases with frequency for a fixed modal order. Table 2.2 lists the general notations used by RST about resonance frequencies. For certain wave families the numerical label l is substituted by a particular symbol. In the following, these notations will be used: $l=S_m$ for the m-order Symmetric Lamb-type waves, $l=A_m$ for the m-order Asymmetric Lamb-type waves, $l=A$ for the Scholte-Stoneley waves [2]. The following equation explains the meaning of the order n of a circumferential wave resonance:

$$n\lambda_{l,n} = 2\pi a \qquad\qquad (2.2)$$

Present investigations are carried out on the TF modulus or spectrum of a scatterer, because resonance location in frequency is the information of concern. Studying how the scattered TF modulus behaves when one or more parameters vary in a selected range is of great interest for interpreting resonance phenomena, identifying their significant features, and formulating mathematical relations between these features and the parameters of interest.

Definition	Symbol
Resonance frequency of family l and order n	$f_{l,n}$ (or $k_{l,n}a$ if dimensionless)
Wave number	$k_{l,n} = \dfrac{2\pi f_{l,n}}{c}$
Wavelength	$\lambda_{l,n}$
Group speed	$c_{l,n}^{gr}$
Phase speed	$c_{l,n}^{ph}$

Table 2.2. Symbols referred to resonance frequencies and to their main properties.

Investigation starts from a reference case consisting of scattering by a steel air-filled shell immersed in salt water and insonified at broadside; the target outer radius is fixed to 25 cm. From [9] it is clear that scattering by thick and thin walled shells is characterized by different physical phenomena. For this reason scatterers can be classified in terms of their wall thickness. The bounds reported in Table 2.3 are adopted here [9]. The boundary between the thin and thick classes is not well defined, so an intermediate case is included which is difficult to investigate and interpret, because phenomena characterizing each of the two main cases may be indistinguishable.

Thickness classification is fundamental to data interpretation. It can be achieved by analyzing the background (non-resonant) scattering component of the target response, which is beyond the scope of this work. It may be useful to recall that in the case of air-filled objects in water:

- a very thin walled shell (quasi a bubble in the limit case) corresponds to an acoustically soft target, characterized by output phase inversion with respect to that of the incident pulse and very low energy at low frequencies (about $ka<5$), and

- a very thick walled shell presents a quasi-rigid background, where the incident pulse phase and spectral shape at low frequencies are maintained in the response specular echo.

The RST takes into account different models of rigid and soft target backgrounds [2], and an intermediate case is also considered [10].

On the basis of these considerations, two distinct analysis and interpretation procedures (one for solid and very thick walled shells, the other for thin walled shells) are needed. Here we focus on the analysis of thin walled shell targets at broadside.

Relative thickness h	Inner radius b [cm] (given a=25 cm)	Object classification
$h \in (0,0.03)$	$b \in (24.25,25)$	Thin walled shell (a bubble in the lower limit case). Quasi-soft or soft background (inversion of the specular-echo phase)
$h \in [0.03,0.12]$	$b \in [22,24.25]$	Intermediate shell
$h \in (0.12,1)$	$b \in (0,22)$	Thick walled shell. Quasi-rigid or rigid background
h=1	b=0	Solid object. Quasi-rigid or rigid background

Table 2.3. Ranges of shell wall thickness.

2.1 Feature selection and physical interpretation

Figure 2.1 presents a case which is taken as a reference for the interpretation of scattering phenomena. It consists of the simulated TF modulus $|H(ka)|$ of a water-loaded, steel, air-filled thin walled shell with fixed outer radius a and variable inner radius b ($b \in [22,25)$ cm, sampling step $\Delta b = 0.1$ cm, i.e., $\Delta h = 0.004$).

The investigated frequency range is $f \in (0,50]$ kHz, which corresponds to $ka \in (0,51.6370]$ given the outer radius fixed to 25 cm and the outer medium sound speed equal to 1521 m/s. Notice that in this case, dimensionless ka values roughly correspond to frequency f values expressed in kHz.
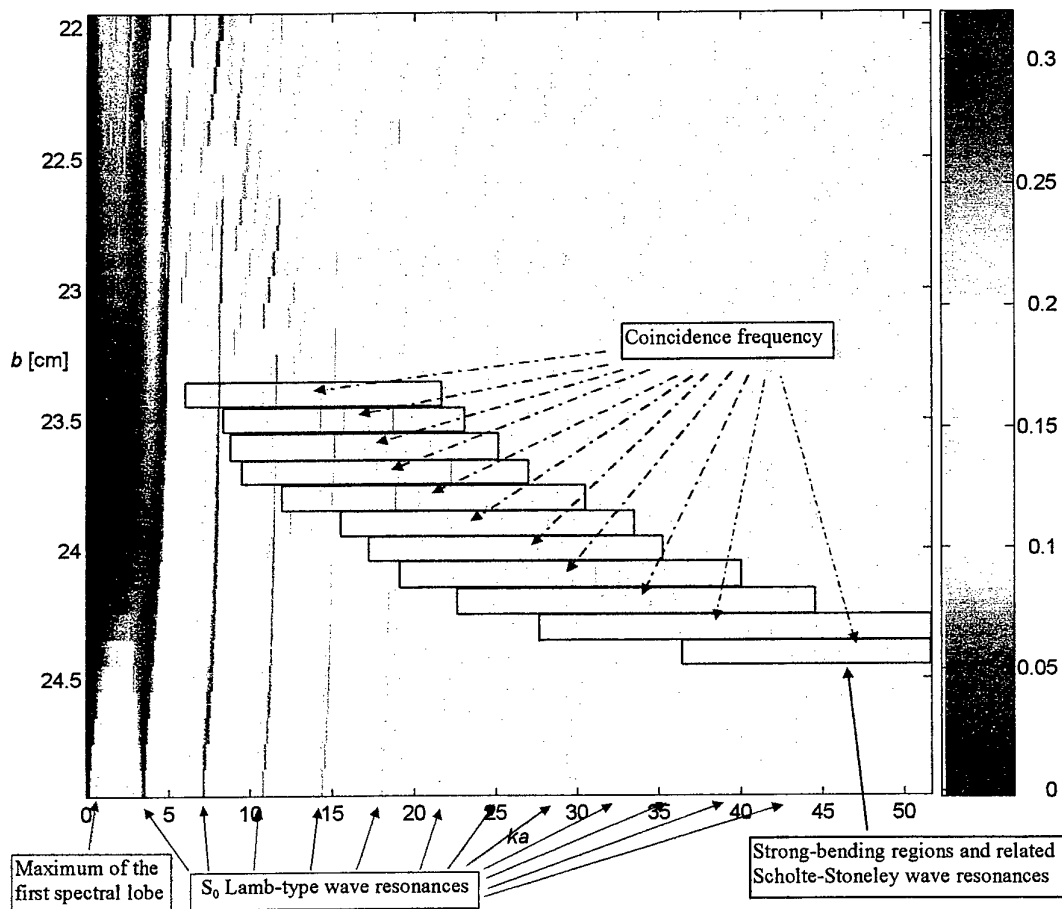
Fig. 2.1. Scattering TF modulus $|H(ka)|$ of a steel, air-filled, thin walled shell in sea water; a=25 cm, b∈[22,24.9] cm, Δb=0.1 cm (Δh=0.004). Some examples of features are outlined.

We can see that for this loading case at broadside, thicker walled shells lead to increasingly more complicated TF patterns, which in turn creates difficulties in detecting and identifying resonance features. In the examined frequency range the TF of a thin

walled shell possesses few resonance characteristics, which are easy to detect and identify in the noise-free ideal case.

The following subsections describe specific features in Fig. 2.1 which are considered significant for target parameter estimation.

2.1.1 Lamb-type waves

The Lamb-type waves are circumferential waves revolving around a thin-walled target. They travel in the target material at the interface with the outer medium. The properties of the waves generated in a cylindrical, thin walled shell (i.e., a circular-cylindrical layer), which is in contact with a liquid on the outer surface and is free (or in contact with air) on its inner interface, are similar to the properties of the normal Lamb waves generated in a dry, plane, thin layer under the same hypotheses of thickness and physical properties [2]. Both symmetric (denoted by S_m) and asymmetric (denoted with A_m) waves are generated.

The *symmetric Lamb-type waves of order* 0 (S_0) are analyzed here as evident in the shell TF at low-intermediate frequencies. They are usually generated in the frequency range $ka \in (5,30)$ and identifiable as distinct, sharp, equally-spaced dips in the TF modulus. For very thin walled shells they are among the most evident resonance features and the easiest to detect and identify in the examined frequency range (see Fig. 2.1).

Their location in frequency is roughly maintained as thickness and the properties of the outer medium vary, while it depends on the shell material parameters c_s and c_p. Moreover, their locations depend on the outer radius in the f domain, but are approximately fixed in the ka domain. Their location in frequency varies with the aspect angle, but remains roughly constant for more than $10°$ from normal incidence [2]. Consequently, they can be used for shell material estimation, given the outer radius.

The asymmetric 0-order family A_0 should be subsonic (i.e., it should have a phase velocity lower than the outer fluid wave speed c) from very low frequencies to a certain frequency, called the coincidence frequency, and should be supersonic at higher frequencies [11]. However, it is damped very quickly, so its contribution is very weak.

The coincidence frequency is so-called for the coincidence (at least approximately) of the A_0 phase speed with that of another resonance family, the Scholte-Stoneley waves [12]. It appears in the range $ka \in (0,50]$ only under certain conditions of thickness and outer medium.

2.1.2 Scholte-Stoneley waves

The *Scholte-Stoneley waves*, also called A waves [2], are fluid-born and travel around the target cross-section with a phase speed always lower than c but asymptotically approaching c (and the A_0 phase speed) near the coincidence frequency. When the dispersion curve of the Scholte-Stoneley phase speed approaches the phase dispersion curve of the A_0 Lamb-type waves, the TF amplitude increases and reaches its maximum

at the coincidence frequency, where the two phase speeds approximately coincide. This means that at the coincidence frequency the two types of waves travel in phase.

At higher frequencies, the A_0 wave phase speed further increases, hence deviating from the Scholte-Stoneley wave phase speed, which remains subsonic. This causes a gradual TF amplitude decrease [13]. The frequency range characterized by the mentioned energy enhancement is called the *strong-bending region* (see Fig. 2.1).

As the A_0 wave resonances provide very weak energy contribution, we identify the equally spaced very sharp discontinuities at the beginning of the strong-bending region and the smooth peak-dip pairs around the coincidence frequency as generated by the Scholte-Stoneley waves.

Given the TF of a certain scatterer, the group speed of the Scholte-Stoneley waves is essentially constant for the detectable resonances as f varies. The distance between adjacent resonances depends strongly on the outer medium and on the outer radius, while it is roughly constant as the inner radius and shell material vary. An overall analysis of Scholte-Stoneley wave characteristics is provided in [12].

The frequency width of the strong-bending domain is nearly constant as a function of the inner radius, but its location varies not only with the outer medium, but also with the shell wall thickness. In particular, it shifts to higher frequencies for thinner walls, and appears at very low frequencies for intermediate thicknesses.

The strong-bending region and the related resonances are particularly evident in the case of thin walled shells, although they may be difficult to detect when they fall at low frequencies where they can interfere with the S_0 Lamb-type resonances, and when walls are so thin that they are beyond the range of interest (i.e., for $ka>50$).

The presence of the strong-bending region at low frequencies can cause uncertainty in the detection of other significant features in the same frequency ranges in intermediate thickness cases; nevertheless, if identified correctly, Scholte-Stoneley wave resonances can be used for estimating the shell **outer radius**. The outer radius of an object is a key parameter, because it allows the estimation of other target geometrical and physical quantities. The accuracy of its estimation strongly influences subsequent estimation steps.

2.1.3 Coincidence frequency

The coincidence frequency, corresponding to the range where the phase speeds of the Scholte-Stoneley and A_0 waves are similar or coincide, presents the maximum energy enhancement in the strong-bending region. It provides another significant feature. It is empirically correlated with the shell wall thickness (see Fig. 2.1), given the outer medium and the shell material shear speed. It is nearly constant with the shell material density and compressional speed. Therefore it can provide a rough estimate of shell wall thickness.

2.1.4 The first spectral lobe

The maximum of the first smooth spectral lobe upper bounded by the first S_0 Lamb-type wave resonance is generally located in the range $ka\sim(0,5)$, as is clear from Fig. 2.1. It seems not to correspond to any resonance, but was empirically seen [2] to depend strongly on the shell wall thickness (i.e., inner radius). Its location depends also on the shell material and on the outer medium, while it remains roughly constant with the outer radius in the ka domain. It can be very hard to detect for intermediate thickness, when its amplitude can be very weak and its location influenced by Scholte-Stoneley waves.

The location of the maximum of the first spectral lobe can be used for **thickness** estimation for very thin walled shells, given the outer radius. However the correlation law between the maximum frequency location and the wall thickness varies as a function of the target material and the outer medium. In addition, its detection is very noise sensitive and not always feasible.

Table 2.4 summarizes the main results of feature selection proposed here.

Feature to extract	Target parameter to estimate	Constraints for matching feasibility
Scholte-Stoneley waves in the strong-bending domain	outer radius a	the strong bending domain falls in the examined frequency range; known outer medium
S_0 Lamb-type waves	shell material	known outer radius
coincidence frequency in the strong-bending region	wall thickness d	the strong bending domain falls in the examined frequency range; known outer medium and shell material
maximum of the first lobe of the TF modulus	wall thickness h	known shell material, outer medium, outer radius

Table 2.4. Low-intermediate frequency resonance features and associated target parameters.

2.2 Matching models for correlating TF features with target parameters

In the following a list of selected theoretical relations and empirical matching models linking resonance analysis with target geometrical and physical parameters is presented and discussed. The models are characterized by:

- analytical simplicity,
- robustness,
- easy applicability to real data.

2.2.1 General theoretical equations

The following equations, as well as Eq. (2.2), are common to any resonance frequency:

$$\frac{c_{l,n}^{ph}}{c} \approx \frac{k_{l,n}a}{n}, \text{ and} \tag{2.3}$$

$$\frac{c_{l,n}^{gr}}{c} \approx (k_{l,n} - k_{l,(n-1)})a. \tag{2.4}$$

They are valid only at normal incidence, otherwise the group and phase speeds generally depend also on the aspect angle.

When a wave l is shear (compressional), the related speeds $c_{l,n}^{ph}$ and $c_{l,n}^{gr}$ converge to the shear (compressional) speed of the target material, as n and ka increases. However, these limits are exact only for large ka values, which are beyond the range of interest.

For low ka values the wave group speed generally varies slowly with ka and n, so that resonances belonging to the same l family can be collected by comparing the distances among pairs of resonance poles in the frequency domain.

2.2.2 Outer radius estimation

For estimating the outer radius from resonance scattering analysis, at least two or three resonance frequencies of the Scholte-Stoneley wave family must be present in the examined frequency range. This is a critical point, as the location of the strong-bending region varies dramatically with wall thickness and material, and with the outer medium. The higher the number of isolated wave frequencies, the higher the robustness and accuracy of the estimate.

The numerical property to extract from these features is the frequency distance $\Delta f_{A,n}$ between adjacent Scholte-Stoneley resonances of orders n and $(n-1)$. Since Scholte-Stoneley resonance frequencies are approximately equally-spaced, an average distance Δf_A computed on a set of distances between adjacent resonances can be used in order to make feature extraction more robust.

Starting from the characteristic that Scholte-Stoneley waves travel around the target in the outer fluid, the following equation between Δf_A and a has been built by equating the Scholte-Stoneley wave group speeds of a reference and an unknown shell,

$$a \approx \frac{cK}{\Delta f_A 2\pi}, \tag{2.5}$$

where K is computed on the basis of a reference case (generally simulated) in which each quantity is known, i.e.,

$$K \approx \frac{\Delta f_{A,ref} \; 2\pi \; a_{ref}}{c_{ref}} \, .$$

(2.6)

A radius estimate can be computed more precisely if c_{ref} is chosen close to c.

An analogous equation involving each resonance frequency instead of its distance from an adjacent resonance can be set. In this case, however, the resonance order is required, which is difficult to determine in real cases.

2.2.3 Shell material estimation

The S_0 Lamb-type waves are well determined and relatively easy to isolate in the ka range (0,20) in the case of very thin walled air-filled shells, for which the strong-bending region is at higher frequencies. From the detection and identification of S_0 frequencies $f_{S0,n}$, and the estimate of the distance $\Delta f_{S0,n}$ between adjacent frequencies of orders n and $(n$-1), properties of the shell material can be estimated from the following equation:

$$c^* \approx c_{S0,n}^{gr} \approx 2\pi \, a \, \Delta f_{S0,n} \, ,$$

(2.7)

where c^* is a parameter identifying the target shell material. It is a combination of the longitudinal and shear speed values:

$$c^* \approx c_s \sqrt{\frac{2}{1-\nu}} \, ,$$

(2.8)

where ν is the Poisson ratio,

$$\nu = \frac{c_p^2 - 2c_s^2}{2(c_p^2 - c_s^2)} \, .$$

(2.9)

When c^* is estimated by Eq. (2.7), the material the characteristic speed of which is the closest to the estimated value is selected as target material. It is clear that the outer radius must be known. A table of c^* values for a set of common materials is given in Annex A.

This approach is derived from an empirical relation which requires order identification, and hence is difficult to use [2]:

$$f_{S0,n} = \frac{n \, c_{S0,n}^{ph}}{2\pi \, a} \approx \frac{n \, c^*}{2\pi \, a} \, .$$

(2.10)

From the equations above one can deduce that the S_0 Lamb-type waves display two significant anomalies: their phase and group speeds roughly coincide and are roughly constant as n and, hence, f vary. This means that their phase and group speeds are nearly non-dispersive, hence an average distance instead of single distances between adjacent resonances can be used in Eq. (2.7) for making the estimate more robust to resonance

measurement inaccuracy. Replacing in Eq. (2.7) $\Delta f_{S0,n}$ with the average Δf_{S0} leads to the following equation:

$$c^* \approx 2\pi\, a\, \Delta f_{S0}, \tag{2.11}$$

which does not require the order identification of the detected S_0 resonances.

2.2.4 Shell thickness estimation

According to empirical tests presented in [2], a relation links the shell wall thickness h with the dimensionless-frequency location $k^{ml}a$ of the first maximum of the scattered spectral response, once the shell material is estimated. This relation is sensitive to the parameters of the fluid surrounding the target.

In this work an analytical statistical model matching the selected feature and the target wall thickness is developed for a steel target in sea water. On the basis of a set of measurements of the selected feature extracted from simulations as thickness h varies (from Fig. 2.1), the true unknown relation $F_o(\cdot)$ between the two quantities is modeled as a polynomial function $\hat{F}(\cdot)$ in a least-squares sense [14] (see Fig. 2.2 (a)). The least-squares method provides also two error bounds that define the confidence interval corresponding to a given confidence level $(1-\alpha)$.

In the present application α is set to 0.5, hence, with reference to Fig. 2.2 (b), if the errors in the measured data are iid normal with constant variance the true parameter value lies within the two red curves defined as $\hat{F}(k^{ml}a) \pm \delta(k^{ml}a)$ with 50% probability:

$$P\{\hat{F}(k^{ml}a) - \delta(k^{ml}a) < F_o(k^{ml}a) < \hat{F}(k^{ml}a) + \delta(k^{ml}a)\} = 0.5. \tag{2.12}$$

(a)

(b)
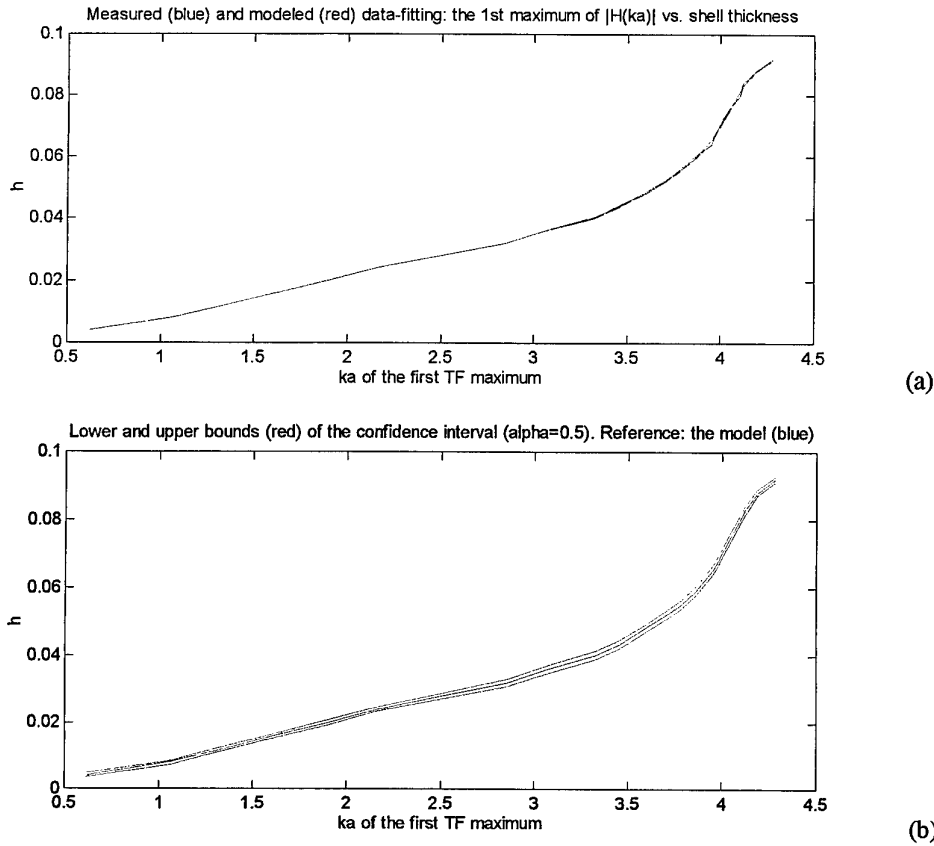
Fig. 2.2. (a) Analytically modeled data fitting between the frequency $k^{ml}a$ of the first maximum of the scattering TF spectrum and the wall thickness h. Polynomial order = 14. (b) Bounds (red) of the model confidence interval as $k^{ml}a$ varies, given the confidence level $(1-\alpha)=0.5$.

A second method for thickness estimation starts from the localization of the maximum energy peak f^{me} inside the strong-bending region, i.e., of the coincidence frequency.

In [13] an empirical relation is proposed for thin, air-filled, aluminum, steel and similar shells:

$$k^{me}a \approx \frac{a}{a-b} = \frac{a}{d} \tag{2.13}$$

from which the following formula, independent from a, directly follows:

$$d \approx \frac{c}{2\pi f^{me}} \tag{2.14}$$

2.2.5 Summary of the selected analytical models

In order to provide the reader with an operative reference, Table 2.5 lists the selected models which will be used in the rest of this section and in Section 4. Only the analytically simplest formulas and those requiring the least number of inputs are used.

Feature to extract	Target parameter	Analytical formula	Reference
mean distance Δf_A between adjacent Scholte-Stoneley resonances	outer radius a	$a \approx \dfrac{c\,K}{\Delta f_A\,2\pi}$	Eq. (2.5)
		$K \approx \dfrac{\Delta f_{A,ref}\,2\pi\,a_{ref}}{c_{ref}}$	Eq. (2.6)
mean distance $\Delta f_{S0,n}$ between adjacent S_0 Lamb-type resonances	shell material from its characteristic speed c^*	$c^* \approx 2\pi\,a\,\Delta f_{S0,n}$	Eq. (2.11)
ka location of the maximum of the first spectral lobe	wall thickness h	Empirical curve, statistically fitted with a polynomial	Fig. 2.6
coincidence frequency f^{me}	wall thickness d	$d \approx \dfrac{c}{2\pi\,f^{me}}$ (aluminum and similar)	Eq. (2.14)

Table 2.5. Summary of selected analytical relations matching features and target parameters.

2.3 Model of a reference scattering response

Section 2.2.2 (see Eq. (2.5) and Eq. (2.6)) has shown that for estimating certain parameters (in particular the outer radius) a reference known scattering case must be used.

Figure 2.3 plots the ideal TF modulus of a steel air-filled shell with a=25 cm, b=24.4 cm. In this case d=6 mm and h=0.024, hence the shell walls are classified as thin. The sound speed in sea water is set to 1521 m/s; Annex A provides the values of the parameters characterizing steel. The plot represents a slice of Fig. 2.1, and the selected features are outlined.

Table 2.6 presents the values of the properties extracted from the selected features. These will be useful as references during the analysis of scattering from unknown targets. The true values of the selected parameters present the subscript 'o'.
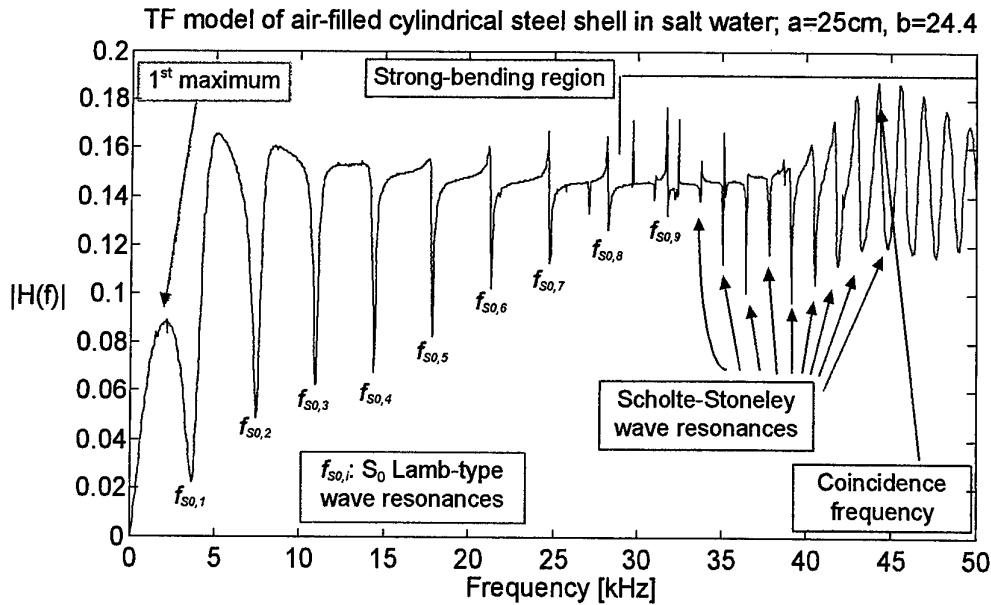
Fig. 2.3. Simulated scattering by an air-filled, steel shell at broadside in sea water.

Feature	Numerical characteristics	True parameter	Formula
Strong-bending region	coincidence frequency inside the region: $f^{me} \sim 44.23$ kHz	$d_o = 6$ mm	Eq. (2.14)
Scholte-Stoneley waves	$f_A = [25.73 \quad 26.953 \quad 29.6875 \quad 31.0058$ $32.3730 \quad 33.6914 \quad 35.0586 \quad 36.4258$ $37.7442 \quad 39.1113 \quad 40.4785 \quad 41.8457$ $43.2617 \quad 44.7754 \quad 46.2402 \quad 47.6075$ $48.9746]$ kHz mean distance between the most reliable resonances: $\Delta f_A = 1.3467$ kHz	$a_o = 25$ cm	Eq. (2.5)
S_0 Lamb-type waves	$f_{S0} = [3.6621, \ 7.4707, \ 10.9375, \ 14.4043,$ $17.8711, \quad 21.3379, \quad 24.7559, \quad 28.2715,$ $31.6895, 35.1565]$ kHz mean distance between adjacent resonances: $\Delta f_{S0} = 3.4668$ kHz	$c_o^* = 5435$ m/s Material = steel	Eq. (2.11)
The first smooth spectral lobe	maximum frequency location $f^* = 2.112$ kHz	$h_o = 0.024$ $b_o = 24.4$ cm	Fig. 2.2

Table 2.6. Features from the reference TF spectrum and related scatterer parameters.

In particular, from the localization of the Scholte-Stoneley resonance frequencies, the constant quantity K (useful for outer radius estimates according to Eq. (2.5)) can be deduced Eq. (2.6). It will be used during data processing in Section 4.

The distances between adjacent resonances computed from the set of Scholte-Stoneley waves included in Table 2.6 are:

$$\Delta f_{A,ref} = [1.3183 \quad 1.3672 \quad 1.3184 \quad 1.3672 \quad 1.3672 \quad 1.3184 \quad 1.3671 \quad 1.3672$$

$$1.3672 \quad 1.4160 \quad 1.5136 \quad 1.4648 \quad 1.3673 \quad 1.3671] \quad kHz \qquad (2.15)$$

The most reliable measurements are the first ten resonances, corresponding to more sharp discontinuities; their mean distance is 1.3467 kHz, which is taken as a reference. Hence the dimension-less reference quantity K can be computed from Eq. (2.7):

$$K = \frac{1346.7 \; 2\pi \; 0.25}{1521} = 1.3904 \qquad (2.16)$$

From the distances computed in Eq. (2.15) the dispersive curve of the Scholte-Stoneley-wave group speed can be easily estimated by means of Eq. (2.4). Its plot, presented in Fig. 2.4, presents a peak around the coincidence frequency, which is confirmed by other authors (e.g., [15]). Figure 2.5 plots the computed dispersion curve of the phase speed of the Scholte-Stoneley wave resonances outlined in Fig. 2.3 and provided in Table 2.6.
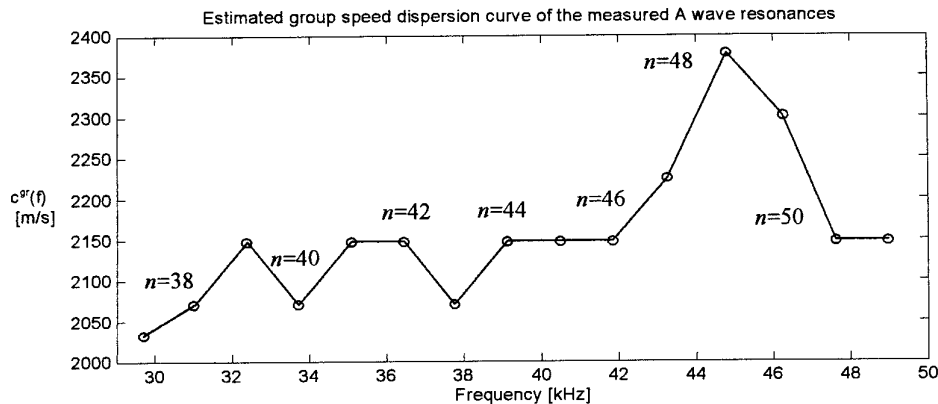
Fig. 2.4. Plot of estimated group-speed dispersion curve of measured A wave resonances. The dots correspond to the measured resonances (some estimated values of order n *are included).*

Assuming that the Scholte-Stoneley wave phase speed at the coincidence frequency approaches c but always remains less than it, the order of the Scholte-Stoneley resonance closest to the coincidence frequency can be approximated by using Eq. (2.3):

$$n^{me} \geq \left\lfloor (k)_{A,n}^{me} \, a \right\rfloor , \qquad (2.17)$$

The symbol "⌊ ⌋" denotes the "integer part of". The order n is deduced from n^{me} estimate.

Estimated dispersion curve of the A wave (blue) and its asymptotic line (red)

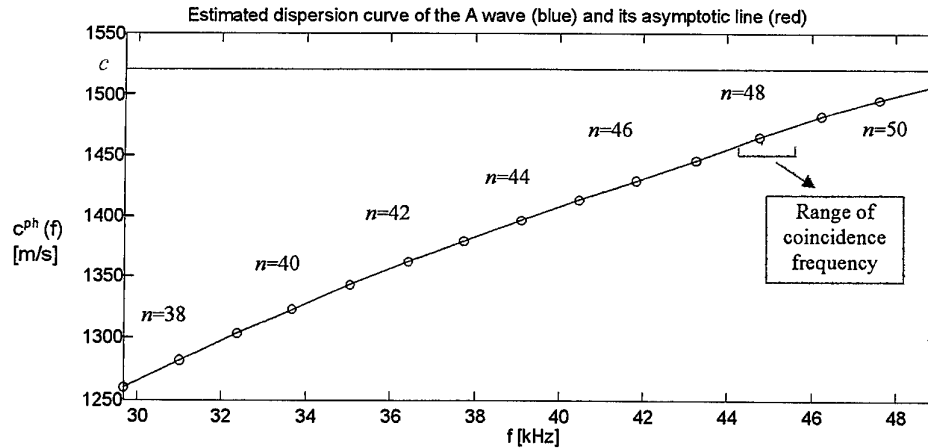*Fig. 2.5. Plot of estimated phase speed of the measured A wave resonances. Some of the estimated wave orders are associated to related measurements (corresponding to the dots).*

From the ka locations of the first S_0 Lamb-type waves, the related phase and group speeds (which are similar in the case of S_0 Lamb waves) are estimated. Figure 2.6 presents the corresponding dispersion curves, which are almost non-dispersive as in the case of Lamb wave propagation in plates [16], except in the low-frequency range where dispersion becomes more significant. The plot suggests application of Eq. (2.10) and Eq. (2.11) on features (frequency location or distance) not involving the S_0 waves with $n=1,2$.

Estimated phase (blue) and group (red) speeds of S0 Lamb-type waves (orders are included)
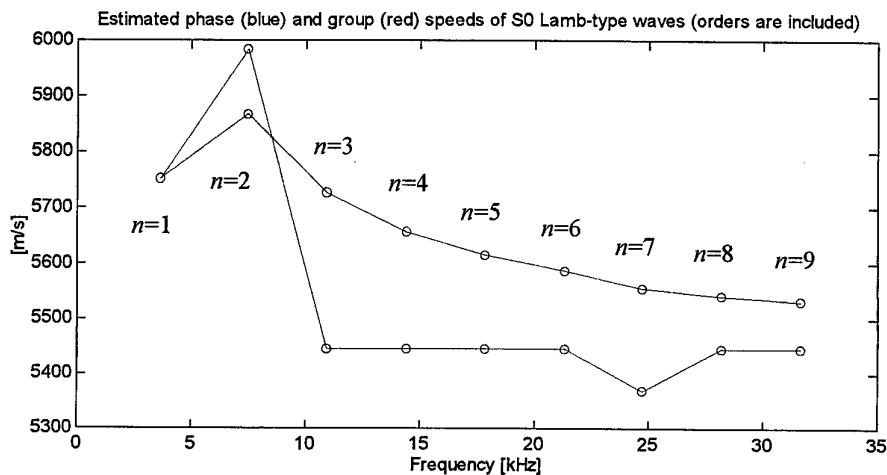

Fig. 2.6. Plot of estimated group and phase speeds of the first S_0 Lamb-type resonances. The two curves tend to the same value as n and f increase.

3

Autoregressive Moving Average (ARMA) -based methods of data representation

3.1 ARMA-based parametric approaches to data representation

In Section 2 the scattering response of an elastic object in the far field has been represented according to the normal-mode strategy adopted by RST [2] as *the linear superposition of an infinite number of modes*, each characterized by a frequency-dependent coefficient (see Eq. 2.1). Each coefficient has been represented as the ratio of two determinants depending on all the geophysical properties of the scatterer. In [2] the modal resonances have been proved to correspond to the *poles* of each coefficient.

Since most of the features selected in Chapter 2 as significant for target characterization are based on the detection and localization of resonances, a useful method for representing scattered data must take into account (and possibly emphasize) the presence of the eventual resonances generated by acoustic scattering. A possible solution is describing the scatterer as a Linear Time-Invariant (LTI) discrete-time system and representing its TF with a parametric model. Parametric modeling consists of choosing an appropriate model depending on unknown parameters, estimating the parameters and substituting the estimation to the system TF.

On the basis of these considerations derived from RST, the models discussed here are the *rational TF* models, which provide explicitly the estimate of the set of TF poles in the z plane. Resonances are defined as those poles of the TF of a LTI discrete-time system that lies on the unit circle in the z-domain.

In this kind of model an input driving sequence $u[k]$ (where $k=1,...,N$ denotes the discrete time index) and the corresponding output series $y[k]$ that must model the data are related by the linear constant-coefficient difference equation,

$$\sum_{l=0}^{p} a[l]y[k-l] = \sum_{l=0}^{q} b[l]u[k-l],$$ (3.1)

with $a[0]=1$. This most general linear model (with both the orders p and q different from 0) is called Autoregressive Moving Average (ARMA). Particular ARMA cases are the autoregressive (AR) model if $q=0$, and Moving-Average (MA) model if $p=0$ [17][18].

The properties of LTI systems for which input and output sequences satisfy a linear constant-coefficient equation such as Eq. (3.1) are best described by the z-transform relationship

$$\left(\sum_{l=0}^{p} a[l]z^{-l}\right)Y(z) = \left(\sum_{l=0}^{q} b[l]z^{-l}\right)U(z)$$ (3.2)

where

$$z = e^{j\omega} \tag{3.3}$$

if a unit sampling interval is assumed.

Hence, the system Transfer Function H(z) for the process of Eq. (3.1) is the rational function:

$$H(z) = \frac{B(z)}{A(z)}, \tag{3.4}$$

where A(z) is the z-transform of AR branch (denominator)

$$A(z) = \sum_{l=0}^{p} a[l]z^{-l}, \tag{3.5}$$

and B(z) is the z-transform of the MA branch (numerator)

$$B(z) = \sum_{l=0}^{q} b[l]z^{-l}. \tag{3.6}$$

It is assumed that A(z) has all its zeros within (or, at least, on) the unit circle of the z-plane. This guarantees that H(z) is stable (asymptotically, if one or more zeros lie on the unit circle) and causal. The TF poles lying on the unit circle correspond to the resonance frequencies generated by the system itself. Since a real impulse response is to be modeled, all complex poles (or zeros) included in the TF rational pattern imply the presence of their respective complex conjugate values among the poles (or zeros). Figure 3.1 shows the poles and zeros of a rational TF in the z-plane. In this example the system is asymptotically stable because of the presence of two couples of complex-conjugated poles on the unit circle.
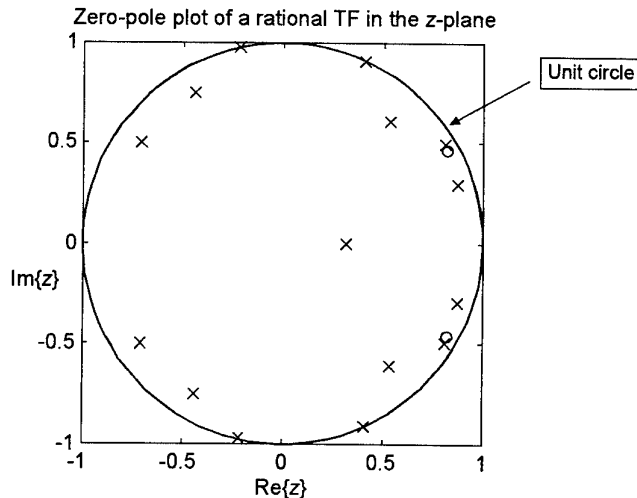

Fig. 3.1. Example of z plot of a generic rational TF (crosses correspond to poles, circles to zeros).

ARMA modeling is particularly useful for representing signals characterized by a set of very tight peaks in the frequency domain, as it can provide more accurate spectral estimates of peaked functions than FFT-based non parametric methods [18][19]. This improvement in frequency resolution is determined by the ability of this approach to fit an assumed model with a relatively small number of parameters [17].

3.2 ARMA models applied to acoustic scattering

From the theoretical analysis of acoustic scattering by RST [2][20], it is clear that a scattering frequency response presents both *poles and zeros*. While poles are fundamental for extracting resonances, zeros generally influence the spectrum global shape. In addition, some zeros correspond to the frequencies of the generated creeping waves traveling around the target in the surrounding fluid. This means that the best scattering model is of the ARMA type. Nevertheless, from the results of feature selection proposed in Section 2, present attention is limited to detecting and accurately localizing the resonances. In this case, AR models are addressed as they are more straightforward to optimize.

A crucial aspect linked with ARMA modeling optimization is the determination of the polynomial orders p and q [17], which depend on the spectral shape of the input/output signals involved, and strongly influence the accuracy of the designed models.

With reference to AR-based modeling only, the *order p* must be estimated, which is a particularly critical parameter, as it is strongly influenced by the *number of resonances* generated by the system [2]. When the TF bandwidth is broad (or theoretically unlimited), p depends also on the selected frequency range of the bandwidth one decides to investigate. Taking into account the frequency range $ka \in (0,50]$ implies observation of a limited number of resonances.

In the literature, various methods exist [17][18][19] to optimize the polynomial orders. A *cross validation* method [18] is used here for comparing different AR-model structures as p varies. The method for selecting the optimal structure among a certain number of possible choices is the well-known Akaike's Information theoretic Criterion (AIC) [18]. It consists of the minimization of a cost functional with respect to the parameters of the structure. It requires the user to suggest possible ranges of variability of the structure.

Once the kind of parametric model (AR, MA or ARMA) and its polynomial order(s) are fixed, many parameter estimation algorithms exist for building the optimal representation of the examined signal sequence. In the present work, focused on modeling a system on the basis of known output and input data sequences, the least squares method is used [17][18].

Finally, it is useful to recall that if a non-parametric FFT-based spectral representation is used instead of a parametric method, resonances can be localized as those frequencies at which π-jumps occur in the signal spectrum phase [2]. Nevertheless, this procedure is generally less accurate and less robust than the AR-based approach, owing to the usual complexity of phase shapes.

4

Application of analysis to data scattered by a cylindrical shell

By using the AR-based methods of resonance extraction and localization (Section 3) and the analytical relations developed for parameter estimation (Section 2), the processing steps presented in Fig. 4.1 were selected and applied to simulated and real acoustic scattering responses of air-filled thin steel shells to normal incident pulses.

Two AR-model-based approaches are selected for data processing:

a)   In the first, a preliminary non-parametric deconvolution phase is applied to the time response in order to recover an approximate impulse response (and corresponding TF) of the scattering system. Deconvolution requires as input a replica of the incident pulse, and is computed in a selected frequency range in which SNR is high in order to limit noise-increasing effects typical of deconvolution (the range [0.5,46] kHz is used in this application). The selection of the best bandwidth to apply deconvolution is critical. Notice that the selected features correlated with shell thickness, i.e., the frequency locations of first lobe maximum and the coincidence frequency, are extracted from the TF spectral shape (see Sections 2.1 and 2.2.4), the accurate estimation of which is, consequently, of great importance. AR modeling is then applied to the deconvolved time sequence in order to estimate the scatterer impulse response and TF.

b)   In the second approach, the output response is analyzed without preliminary deconvolution, as the input signal exciting the scattering system is taken into account during the AR-based modeling process, which includes an implicit deconvolution step. In this case, the deconvolution frequency range cannot be controlled. AR-based representation of scattered output data cannot provide the TF spectral shape recovery; hence the capabilities of this approach are more limited, the features that can be extracted from the TF shape are missing, and the related parameters cannot be estimated.

Poles on the unit circle in the z-plane are considered to be resonances. As the location of the poles cannot be estimated perfectly, a finite annulus is defined in the z-plane for which the location of the estimated poles will be considered resonances. For this work the annulus will be such that $0.95 \leq |z| \leq 1$. Figure 4.2 shows an example in the z-plane.

The two approaches are applied to the global scattering response, as well as to its pure resonance [7] and far resonance [5] components.
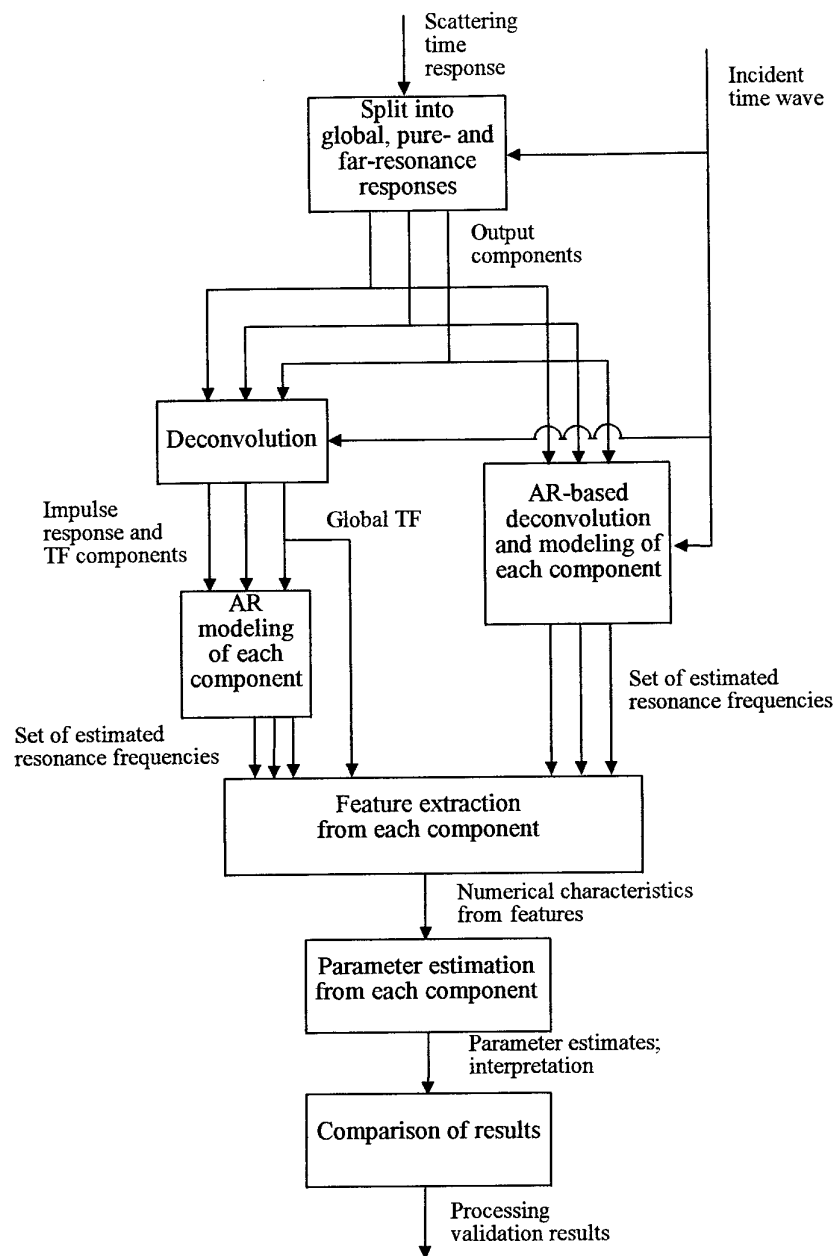
Fig. 4.1. Block diagram of the selected processing steps.
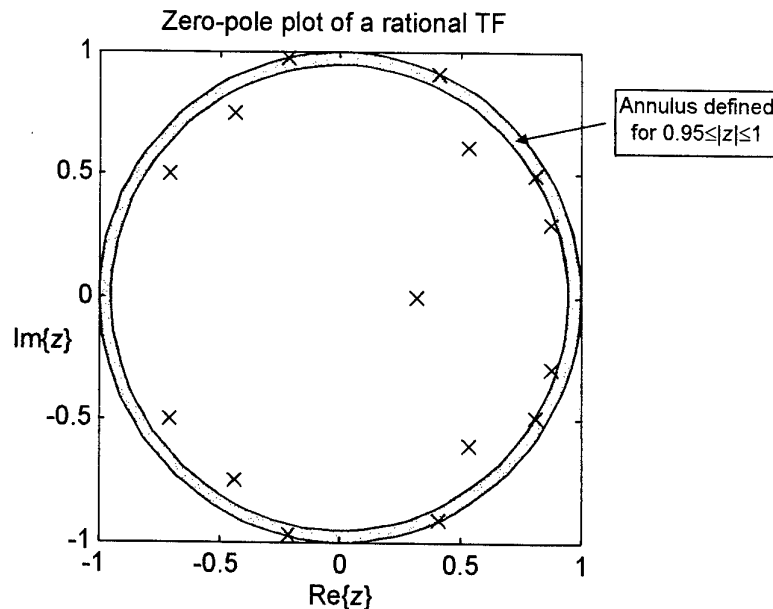
Zero-pole plot of a rational TF

Fig. 4.2. A zero-pole plot and the annulus used for selecting the system resonances among the estimated poles.

The global time response scattered by an insonified object is split into the specular reflection and the pure resonance component by applying the algorithm proposed in [7]. The specular reflection is first estimated and then subtracted from the global response, hence obtaining the pure resonance part. As a consequence, this algorithm takes into account eventual time overlapping of the specular echo with the resonance response. The estimation method consists of an adaptive filtering process based on the Recursive Least Squares learning, which is a linear technique derived from the LMS algorithm. Accuracy in splitting the global response is critical to isolating the resonance peaks in the spectrum of the component obtained.

A time gate is further applied to the pure resonance response in order to isolate the far-resonance component, i.e., the target time response long time after the specular echo arrival [5]. It is characterized by low energy, and in real cases can be insufficiently long for allowing a high-resolution frequency analysis, but it is useful for isolating and, hence, localizing those resonances at intermediate frequencies that can remain partially or completely hidden in the global and pure resonance spectra. Where to apply this second gate is computed by evaluating how the scattered energy varies over time [5]: the low-energy tail of the scattered time sequence far from the specular echo end is selected. If the time series obtained is long enough, the exact time location of the gate is not a critical parameter for resonance-extraction accuracy.

The scattered resonance frequencies are extracted and localized from each component (i.e., the global TF and its pure and far resonance parts), represented and estimated on the basis of an AR model. A subset of resonances is identified and used for estimation as correlated to specific target parameters according to the matching models proposed in Chapter 2. Finally, the estimation results obtained by processing the global, pure and far resonance responses separately are evaluated and compared in terms of accuracy and reliability.

Some examples are presented on which the above processing phases were validated and tested. These examples refer to the trials performed in a dock of the La Spezia Military Arsenal in August 1996. The experimental geometry is sketched in Fig. 4.3. Details about the trial set-up and the presentation, discussion and preliminary validation of data are provided in [3]. Steel circular cylindrical shells with flat ends were used as targets. They are 2 meter long, their outer radius a is 25 cm, their inner radius b is 24.4 cm. As the relative thickness h=0.024 (and d=a-b=6 mm), the shells are classified as thin from Table 2.3. The present analysis addresses an air-filled shell insonified at nominal broadside.
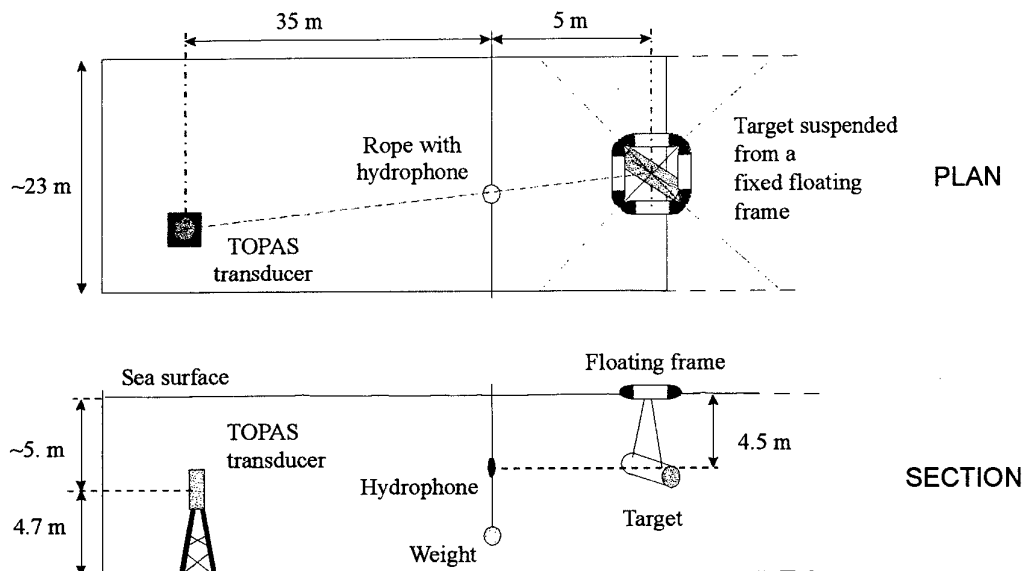

Fig. 4.3. Scheme of the experiment configuration in a basin (not to scale).

The estimated parameters were the shell outer radius, and the wall thickness and material, given the inner and outer media properties and the target shape. Whenever the outer radius could not be estimated, i.e., when the necessary features could not be extracted from data, it was assumed as *a priori* known.

As incident acoustic signals, Ricker pulses with different central frequencies were selected. They were transmitted by a parametric array sonar (TOPAS PS 040) [21]. One particular pulse is used here (see Fig. 4.4). Its frequency-domain plot was obtained by zero-padding before FFT computation in order to show a smoother curve. This technique was applied, when needed, to each time sequence analyzed in this work. The incident pulses and scattered responses were averaged across roughly 100 pings.

The TOPAS generates secondary frequencies in the range [2,16] kHz by transmitting a broad-band pulse near 40 kHz (primary frequency) and using the non-linear properties of water. For this reason, two main spectral components, corresponding to the secondary and primary frequencies, can be seen in the spectrum plotted in Fig. 4.4.

System filters have affected the overall frequency response. However, since the outgoing pulse is recorded on the same system as the scattered data, and the signal path is the same for both, we have all the information needed to estimate the scatterer TF. In the processing phases, even the primary frequency signal component was considered, in

order to be able to test whether it could excite the target resonance scattering in both simulated and real data. Hence, no pre-processing low-pass filter was applied to the scattered data.
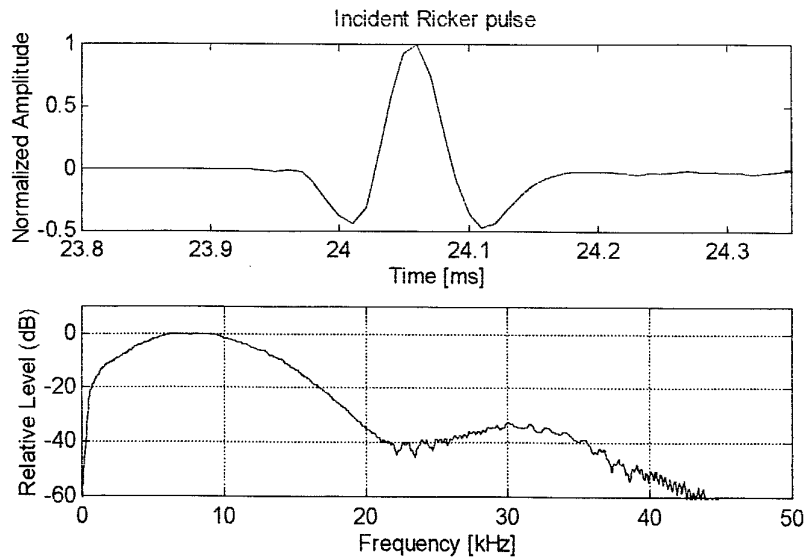

Fig. 4.4. Real incident Ricker pulse (time and frequency domains).

The target response to the selected incident pulse was simulated and used as a reference during the real data analysis [3]. Although this model is not perfectly realistic for the examined application, fitting between simulated and real scattering responses was considered acceptable in the frequency range [4,16] kHz [3]. Good data-model matching was obtained in terms of the TF pattern, extracted features and parameter estimates in the extended range $f \in [4,46]$ kHz.

4.1 Simulated data processing

Analysis of the simulated scattering response to the Ricker pulse (Fig. 4.4) is presented (Fig. 4.5). Figure 4.6 provides the decomposition of the simulated global response into specular echo and pure resonance component, as obtained by the Azimi-Sadjadi algorithm [7]. The far-resonance component is selected by gating the resulted pure resonance response at 25.78 ms, as shown in Fig. 4.7, i.e., sufficiently far from the end of the specular echo, occurring around 24.05 ms.

Feature extraction and parameter estimation results obtained here, together with those provided in Section 2.3, will be taken as a reference for corresponding real data analysis results. These results, obtained under ideal conditions of geometry and absence of noise, are mainly useful for:

1. validating the accuracy of AR-modeling in extracting and localizing all the generated resonance frequencies;

2. validating the adequacy and accuracy of the proposed feature-parameter matching models.
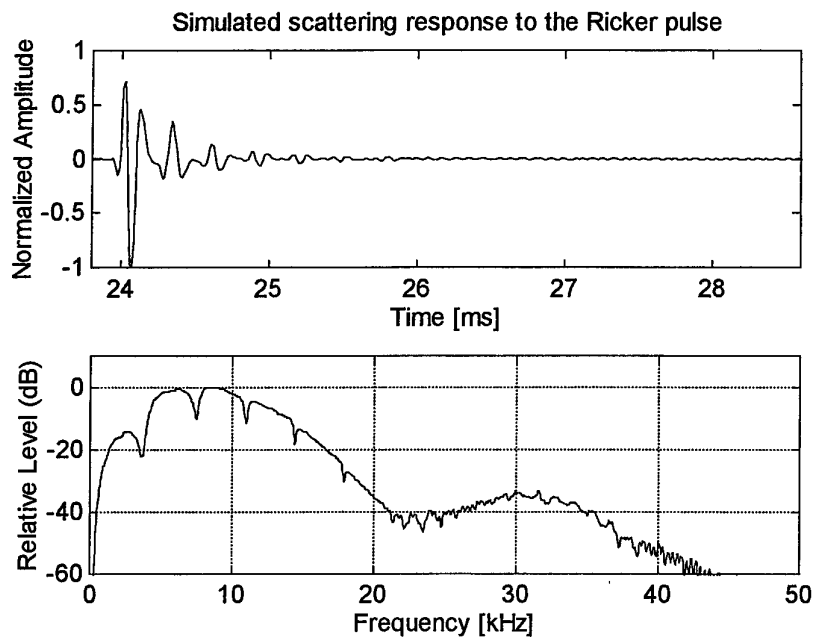
Fig. 4.5. Simulated target response (time and frequency domains).
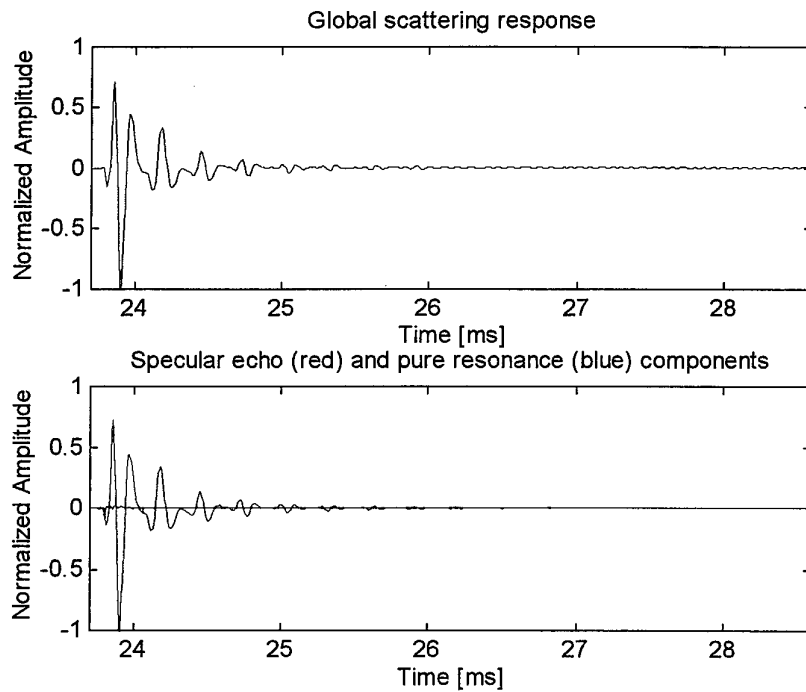
Fig. 4.6. Simulated global response and its decomposition into specular echo and pure resonance component.

Estimated pure resonance response and selection of the far resonance component
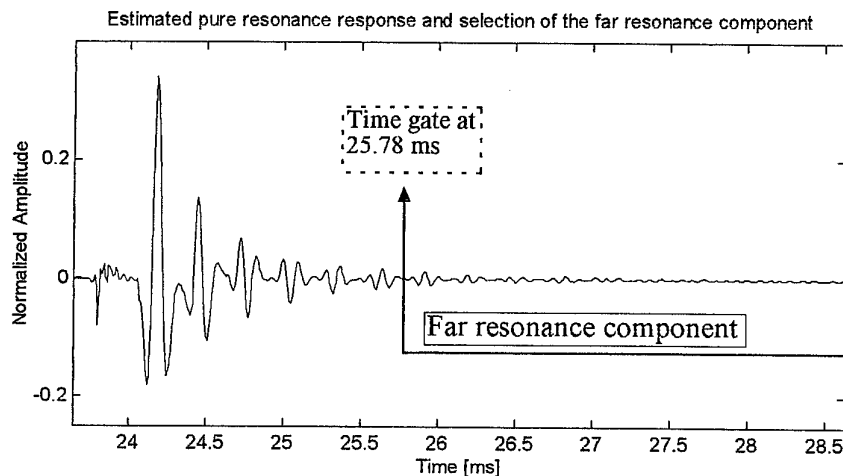
Fig. 4.7. Estimated pure resonance response and selection of the far-resonance part by time gating.

As data are simulated (hence noise-free) on the basis of the selected theoretical model, data-model fitting and noise robustness of deconvolution, resonance-extraction and parameter-estimation methods cannot be tested here.

4.1.1 Analysis of deconvolved scattering response

Approach a) is applied to the global, pure and far resonance components separately. The order of the used AR models are estimated automatically by applying the AIC criterion, as explained in Section 3.

The *global* TF spectrum and phase are considered in Figs. 4.8 and 4.9.

Deconvolved simulated response (blue), extracted resonances (red). Ref.: simulated TF spectrum (green)

Fig. 4.8. Global TF spectrum, resonance extraction (AR order p=80), and reference TF pattern.

Phase of deconvolved simulated response, and selected resonances
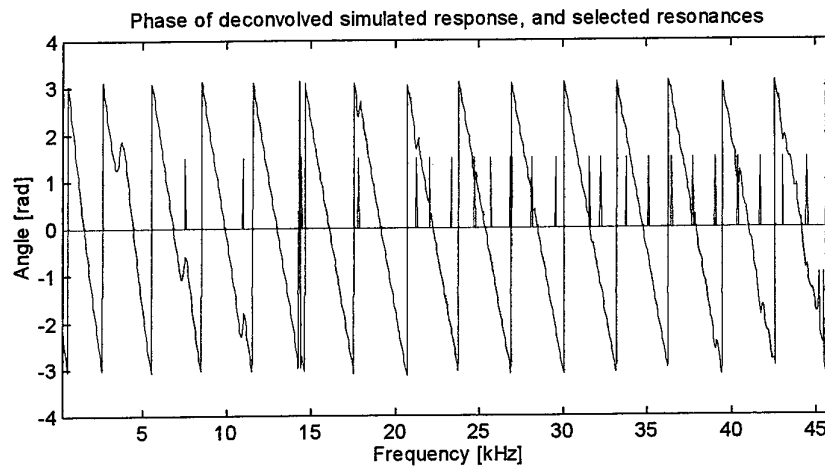
Fig. 4.9. Deconvolved simulated global response (phase component) and matching with selected resonances: the resonances correspond to phase jumps.

Processing the TF amplitude and phase components generally provides redundant results in terms of resonance feature extraction. All the dips/peaks in the spectrum 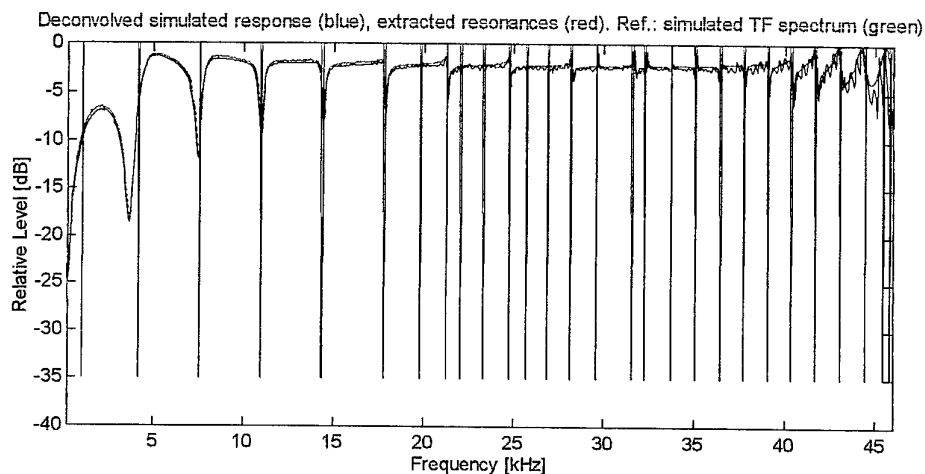of Fig. 4.8 correspond to more or less evident phase jumps shown in Fig. 4.9 [2]. Hence analysis will refer to the spectrum only.

Resonance identification and grouping are presented in Fig. 4.10. Estimation results can be evaluated from Table 4.1, in which estimated parameters are denoted by the symbol '^'. A comparison can be performed with the reference values reported in Section 2 (Table 2.6), derived from the analysis of the scatterer ideal TF.

Deconvolved simulated spectrum (blue), identified S0 Lamb-type (green) and A (red) wave resonances

Fig. 4.10. Deconvolved global spectral response and identification of the selected resonances.

In Fig. 4.8 the resonances at 1.086 and 19.816 kHz are spurious, as deduced both from the absence of corresponding spectral discontinuities and from comparison with the resonance identification provided in Table 2.6. The first-order S_0 Lamb-type resonance is

estimated inaccurately with respect to the spectral dip located around 3.66 kHz, hence disregarded.

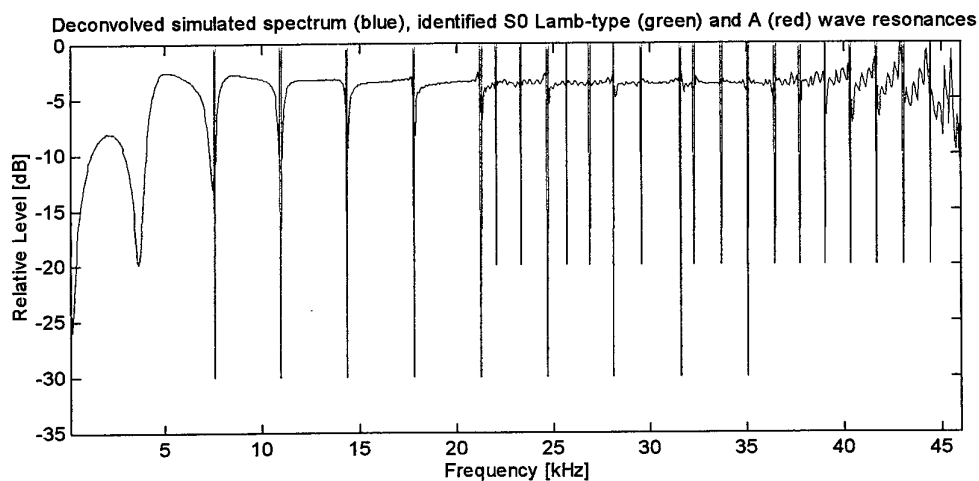Feature extraction and parameter estimation results are good if compared with true values. Hence the approach based on preliminary deconvolution, resonance extraction from AR-model, and RST feature-parameter matching provides a set of accurate estimates, starting from simulated global response to a real broadband pulse.

Feature	Measure of numerical characteristics	Parameter estimate	Parameter true value
Strong-bending region	coincidence frequency $f^{me} \sim 42.92$ kHz	**thickness** $\hat{d} = 5.6$ mm	$d_o = 6$ mm
Scholte-Stoneley waves	frequency locations [kHz]: 22.05, 23.33, 25.740, 26.923, 28.198, 29.597, 32.291, 33.732, 35.099, 36.454, 37.729, 39.054, 40.366, 41.691, 43.042, 44.469; mean distance between adjacent resonances: $\Delta f_A = 1.3467$ kHz	**outer radius** $\hat{a} = 24.99$ cm	$a_o = 25$ cm
S_0 Lamb-type waves	frequency values [kHz]: 7.575, 10.967, 14.383, 17.818, 21.275, 24.736, 28.198, 31.604, 35.099; mean distance between adjacent resonances: $\Delta f_{S0} = 3.4567$ kHz	if a_o is used: $\hat{c}* = 5429.8$ m/s if $\hat{a}$ is used: $\hat{c}* = 5427.6$ m/s **shell material** is *steel*	$c_o^* = 5435$ m/s Material = steel
The first smooth lobe	maximum frequency location $f* = 2.100$ kHz	**thickness** with a_o: $\hat{h} = 0.0242$ $\hat{b} = 24.4$ cm with $\hat{a}$: $\hat{h} = 0.0241$ $\hat{b} = 24.39$ cm in both cases, confidence interval (given the confidence level =50%) = $\hat{h} \pm 0.0005$	$h_o = 0.024$ $b_o = 24.4$ cm

Table 4.1. Analysis of the simulated deconvolved global response.

It is clear that for applying the proposed matching relations and reaching the above estimation results on the examined shell, some constraints on the bounds of the examined frequency range must be imposed. Frequency analysis must be extended at least to $f \cong 46$ kHz, otherwise some features linked to the strong-bending domain (i.e., the Scholte-Stonely wave resonance locations and the coincidence frequency) can be missed, with consequent inability to estimate related target parameters (i.e., outer radius and

thickness). Hence, analysis of only the secondary frequency response ($f<20$ kHz) is not sufficient. Moreover, thickness can also be estimated by analyzing the low-frequency TF pattern. In this case, data must be available starting from at least 1-2 kHz in order to detect the first spectral lobe. This is another constraint imposed by the processing methods used on the selection of appropriate exciting signals and receiver working range. The frequency boundaries imposed for discriminating the selected features inside the examined range vary strongly with all the geophysical and geometric properties of the target and its outer medium, as explained in Chapter 2.

As an aid for refining the global response analysis, the deconvolved *pure resonance* component is taken into account in order to:

1. show how resonances at low-intermediate frequencies are emphasized as evident peaks by isolating the resonance response from the specular echo;

2. select the features whose extraction is feasible even from this partial response;

3. compare the accuracy of the proposed techniques of parameter estimation which can be applied to both global and resonance responses.

Processing results are shown in Fig. 4.11 and Table 4.2. The resonance peaks extracted here correspond to the dips and peak/dip pairs in the global TF spectrum. Note that only resonance features can be extracted. Frequency localization is very accurate, although the first-order S_0 Lamb-type wave resonance is missed again. This phenomenon is expected as this resonance corresponds to the widest and smoothest mode plotted in Fig. 4.11.

The outer radius and the shell material, which are the only two parameters that can be evaluated, are estimated even better than from the global response, simply because resonance features are more prominent. In any case, the difference is very small.

These results suggest that splitting between specular echo and resonance component by means of the algorithm proposed in [7] is successful.
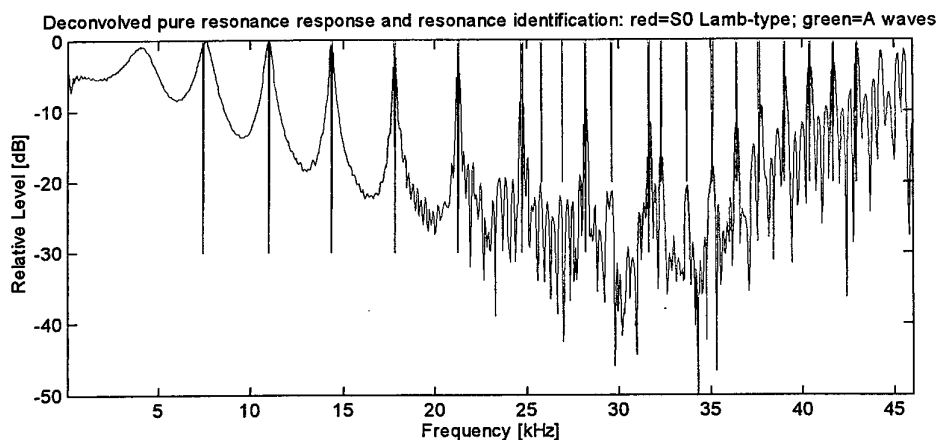

Fig. 4.11. Deconvolved pure-resonance *spectrum, and resonance identification (AR order* p=90).

Feature	Measure of numerical characteristics	Parameter estimate	Parameter true value
Scholte-Stoneley waves	frequency location [kHz]: 25.849, 26.944, 29.628, 32.330, 33.735, 35.094, 36.429, 37.667, 39.081, 40.411, 41.683; mean distance between adjacent A resonances: $\Delta f_A = 1.3465$ kHz	*outer radius* $\hat{a} = 25.00$ cm	$a_o = 25$ cm
S_0 Lamb-type waves	frequency values [kHz]: 7.425, 10.964, 14.383, 17.820, 21.274, 24.732, 28.201, 31.642; mean distance between adjacent resonances: $\Delta f_{S0} = 3.4595$ kHz	shell material speed $a_o = \hat{a}$ is used: $\hat{c}* = 5434.2$ m/s *material* estimate is *steel*	$c_o^* = 5435$ m/s steel shell

Table 4.2. Analysis of the deconvolved pure resonance *component of the response.*

The noise-free *far resonance* component is analyzed for:

1. showing how resonances can be extracted from the time-response tail;

2. selecting the features whose extraction is feasible even from this partial response;

3. comparing the accuracy of the proposed techniques.
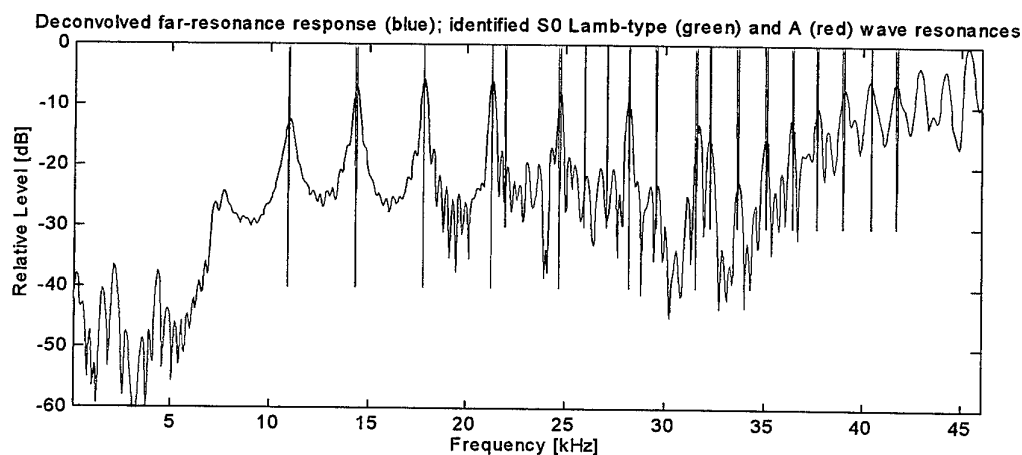
Results are provided in Fig. 4.12 and Table 4.3.

Fig. 4.12. Deconvolved far-resonance *spectrum and identification of resonances (AR order p=85).*

Feature	Measure of numerical characteristics	Parameter estimate	Parameter true value
Scholte-Stoneley waves	frequency location [kHz]: 21.956, 25.974, 27.080, 29.608, 32.256, 33.682, 35.090, 36.461, 37.716, 39.018, 40.449, 41.771, 46.473; mean distance between adjacent frequencies: $\Delta f_A \cong 1.3472$ kHz	*outer radius* $\hat{a} = 24.98$ cm	$a_o = 25$ cm
S_0 Lamb-type waves	frequency values [kHz]: 10.981, 14.383, 17.806, 21.271, 24.728, 28.208, 31.593; mean distance between adjacent frequencies: $\Delta f_{S0} \cong 3.4608$ kHz	shell material speed with a_o : $\hat{c}^* = 5436$ m/s with $\hat{a}$: $\hat{c}^* = 5432$ m/s *shell material is steel*	$c_o^* = 5435$ m/s Material = steel

Table 4.3. Analysis of the deconvolved far resonance *component of simulated data.*

As in the deconvolved pure resonance response spectrum, the resonances correspond to sharp peaks, but the lowest ones are either missed or not very evident. When detected, resonances are localized accurately, hence allowing very good estimation results comparable with those obtained from the pure resonance response. As in the analysis of the pure resonance response, those features related to the TF spectral shape cannot be detected, limiting the number of estimated parameters.

In the pure and far resonance components, peaks corresponding to resonances are emphasized because the specular echo amplitude has been filtered out by the splitting procedure [7]. Ripple effects are evident, but do not influence AR-based resonance extraction.

The further the time gating from the specular echo arrival, the more evident are the resonance peaks at intermediate-high frequencies and, hence, the higher the probability of their detection. Nevertheless, it is clear that a trade-off between far time-gating and high energy level must be considered in order to obtain the optimal resonance extraction results from the resulting far-resonance response.

Comparison of pure and far resonance responses limited to *noise-free* ideal scattering would suggest that one of the two could be omitted, as their results are comparable. While the global response analysis is fundamental for extracting TF-curve features, the resonance response is shown to emphasize the generated resonances and, hence, can eventually refine some of the estimation results based on resonance extraction and localization.

4.1.2 Scattering analysis without preliminary deconvolution

Approach b) provides more limited results than technique a), because it does not provide TF recovery. Nevertheless, it is taken into account in order to test its AR-based capabilities of resonance detection and localization, compared with the previous approach.

The *global response* is analyzed and results are compared with those coming from approach a). Both Scholte-Stonely and S_0 Lamb-type waves are detected, localized and processed.

In Fig. 4.13 the resonance frequencies estimated by means of an AR model with 90 poles are shown. Extracted resonances are matched with the output spectrum and fitted with the reference resonances computed in Section 2.3.

Except for some spurious estimates which correspond to neither spectrum dips nor resonance true values, most of the extracted frequencies fit the S_0 Lamb-type wave resonances of the first few orders. The first dip (i.e., the S_0 Lamb-type resonance of first order) is missed. Some of the expected Scholte-Stoneley wave resonances fit well with selected frequencies. Numerical results are provided in Table 4.4.
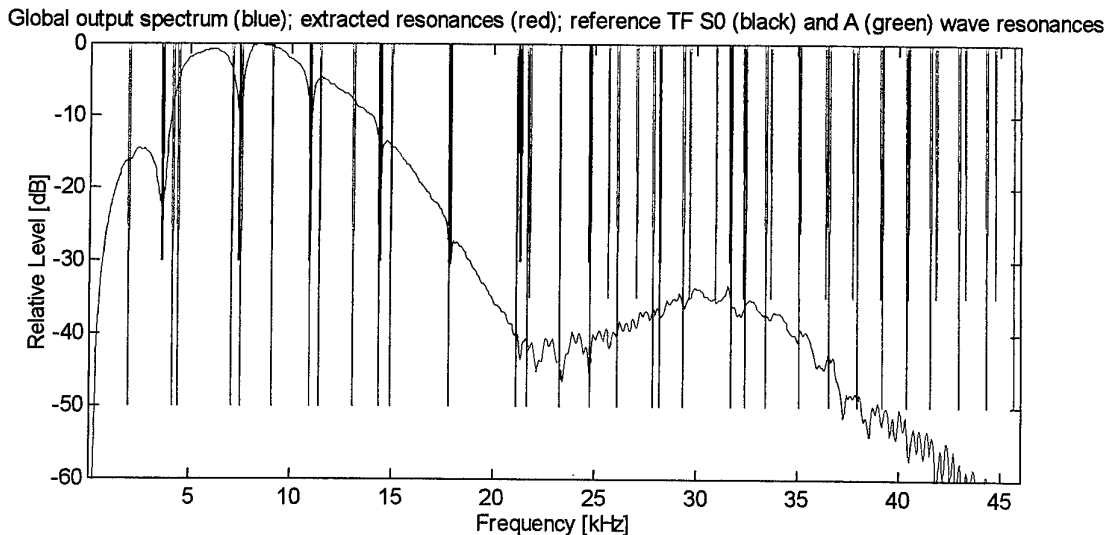
Global output spectrum (blue); extracted resonances (red); reference TF S0 (black) and A (green) wave resonances

Fig. 4.13. AR-based analysis of the global output response (AR order p=90).

Feature	Measure of numerical characteristics	Parameter estimate	Parameter true value
Scholte-Stoneley waves	frequency values f_A [kHz]: 21.711, 29.404, 32.412, 35.124, 37.955, 39.187, 40.438; mean distance between adjacent frequencies: $\Delta f_A = 1.3402$ kHz	**Outer radius** estimate: $\hat{a} = 25.11$ cm	$a_o = 25$ cm
S_0 Lamb-type waves	frequency values f_{S0} [kHz]: 7.586, 10.967, 14.373, 17.815, 21.194, 24.809, 28.243, 31.716; mean distance between adjacent frequencies: $\Delta f_{S0} = 3.4582$ kHz	shell material speed with a_o: $\hat{c}^* = 5432.1$ m/s with $\hat{a}$: $\hat{c}^* = 5456$ m/s **shell material** estimate is steel	$c_o^* = 5435$ m/s Material = steel

Table 4.4. Analysis of the simulated global response to the Ricker pulse.

With reference to the analysis of simulated global-response only, some considerations can be outlined from comparison with approach a):

1. Resonance-feature fitting and consequent parameter estimation results are comparable with those obtained by the deconvolved response (the outer radius estimate is slightly worse, but the shell material estimate has comparable accuracy).

2. Missing the extraction of features linked to TF shape recovery limits the number of estimated parameters.

As a consequence, approach a) appears to be superior to approach b) in the case of simulated global output data.

The *pure resonance response* is analyzed, and results are compared with those coming from the application of approach a) to the same data.

Fig. 4.14 presents the spectrum of the pure-resonance response matched with the modeled TF spectrum.

For f<23 kHz most of the emphasized peaks correspond with TF dips (i.e., S_0 Lamb-type waves), as expected. At higher frequencies, resonance isolation fails in terms of model-data spectral fitting, while providing good results in terms of AR-based resonance extraction and localization (most of the selected resonance lines match with model TF discontinuities in the frequency range [25,45] kHz).

Pure resonance response (blue) and ideal TF (green) spectra. AR-based extracted resonances (red)
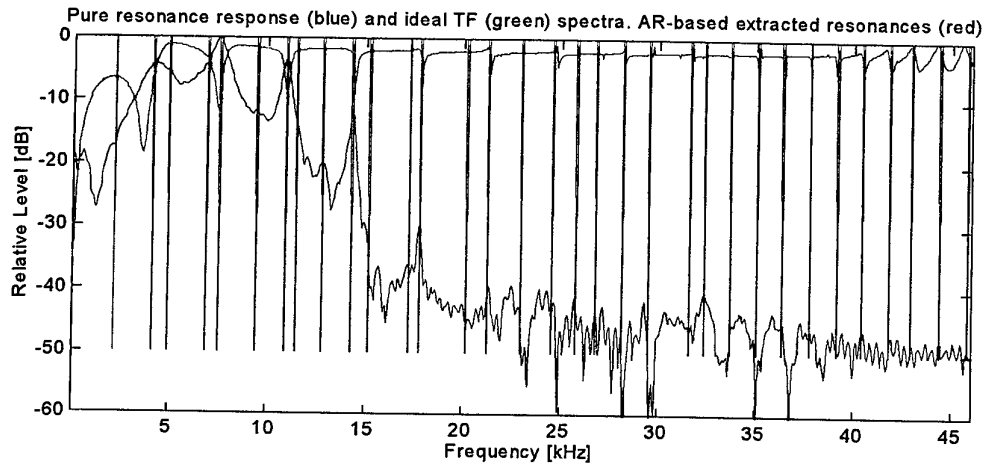
Fig. 4.14. Spectral matching between the pure resonance *response and the TF model (AR order p=80).*

Fig. 4.15 matches the identified estimated resonances with the Scholte-Stoneley and S_0 Lamb-type waves estimated from the analysis of the simulated TF spectrum, which is also plotted as a reference.

Some resonances are mismatched, but many are localized with good accuracy. Numerical results are provided in Table 4.5. Parameter estimates are comparable with those obtained from processing the global response. Hence, analyzing this component further than the global output provides no further information.

Identified S0 (green) and A (red) wave resonances, matched with the ideal TF pattern

Fig. 4.15. Pure resonance *response analysis, referred to the TF model.*

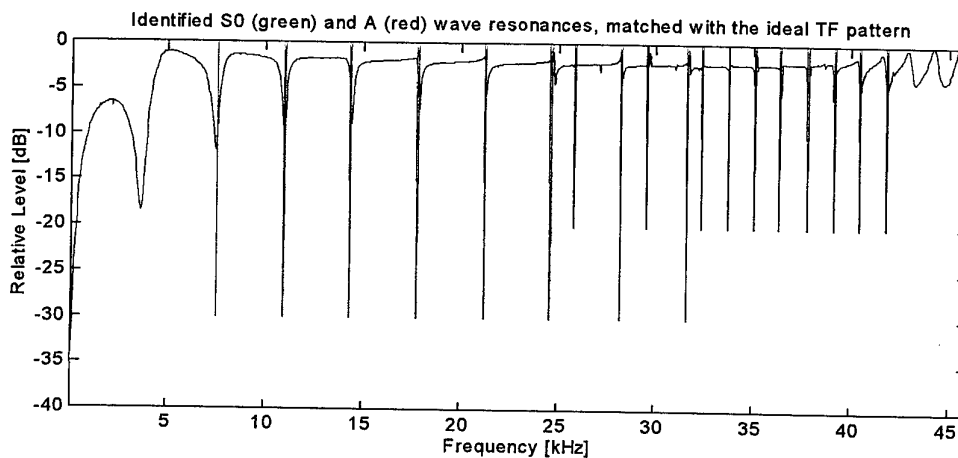| Feature	Measure of numerical characteristics	Parameter estimate	Parameter true value
Scholte-Stoneley waves	frequency values [kHz]: 25.824, 29.538, 32.383, 33.751, 35.101, 36.393, 37.775, 39.219, 40.466, 41.850; mean distance between adjacent frequencies: $\Delta f_A = 1.3525$ kHz	*Outer radius* estimate $\hat{a} = 24.89$ cm	$a_o = 25$ cm
S_0 Lamb-type waves	frequency values [kHz]: 7.589, 10.969, 14.374, 17.831, 21.304, 24.629, 28.245, 31.632; mean distance between adjacent frequencies: $\Delta f_{S0} = 3.4564$ kHz	shell material speed with a_o: $\hat{c}* = 5429.4$ m/s with $\hat{a}$: $\hat{c}* = 5405.5$ m/s shell *material* estimate: steel	$c_o^* = 5435$ m/s Material = steel

Table 4.5. Analysis of the simulated pure resonance *response.*

Compared with results obtained using technique a) on the same component, the estimation accuracy obtained here is only slightly worse. Hence, the two methods applied to simulated data are comparable in terms of accuracy. On the other hand, the capability provided by technique a) of matching extracted resonances with TF peaks is appreciable and improves robustness of resonance selection and identification.

Analysis of the *far-resonance response* isolated from simulated data is now considered, and a comparison with previous results is sketched. In Fig. 4.16 the isolated far-resonance spectrum is matched with the ideal TF spectrum. For $f<10$ kHz matching is poor, and confirms the observations referred to the results of approach a) on the same component. Starting from $f\approx10$ kHz, the emphasized peaks (more evident than those present in the pure-resonance data) match well with the TF spectral dips, at least up to $f\approx43$ kHz.
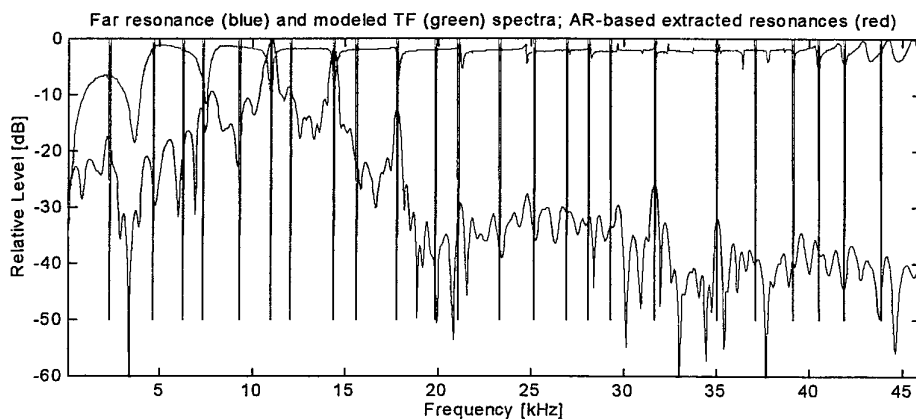
Far resonance (blue) and modeled TF (green) spectra; AR-based extracted resonances (red)

Fig. 4.16. Matching of far-resonance *and modeled TF patterns. AR-based extracted resonances (AR order* p=60).

Extracted (black) and expected (red) S0 waves; extracted (magenta) and expected (green) A waves. Ref. TF (blue)
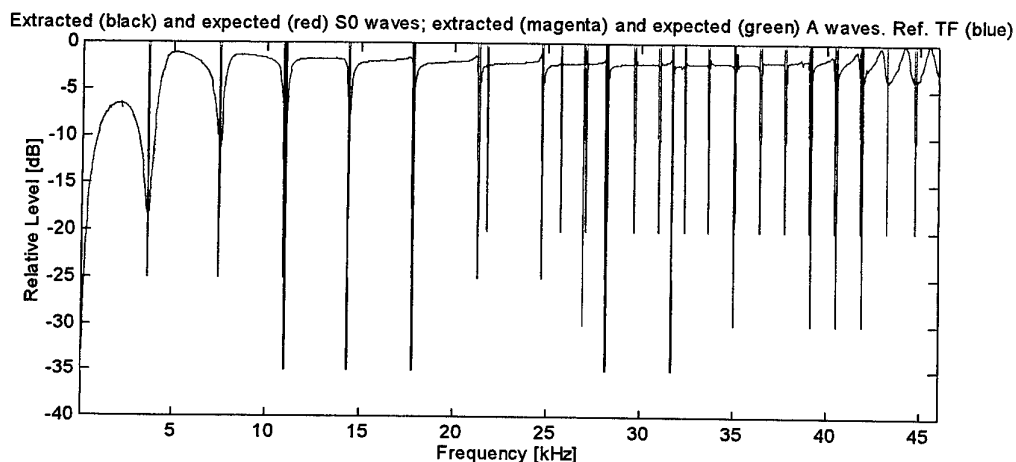
Fig. 4.17. AR-based analysis of the far resonance *response, referred to the ideal TF pattern.*

Fig. 4.17 shows selected and identified S_0 and Scholte-Stoneley wave resonances compared with the related resonances estimated from the ideal TF, the pattern of which is also provided as a reference. Although some resonances are lost (as well as in the analysis of the pure resonance response in Fig. 4.15 above), others are estimated with good accuracy, as confirmed by the numerical results in Table 4.6.

Resonance analysis results of approaches a) and b) on the simulated far-resonance component are comparable in terms of accuracy, although the TF shape matching provided by approach a) makes resonance identification more robust, as already noticed with reference to the other output components.

Feature	Measure of numerical characteristics	Parameter estimate	Parameter true value
Scholte-Stoneley waves	frequency values [kHz]: 26.938, 35.057, 39.174, 40.529, 41.910; mean distance between adjacent frequencies: Δf_A =1.3532 kHz	*Outer radius* $\hat{a}$ = 24.87 cm	a_O =25 cm
S_0 Lamb-type waves	frequency values f_{S0} [kHz]: 10.987, 14.399, 17.820, 28.140, 31.709; mean distance between adjacent frequencies: Δf_{S0} =3.4607 kHz	shell material speed with a_O : $\hat{c}$ *=5436 m/s with $\hat{a}$: $\hat{c}$ *=5408 m/s *shell material* estimate is steel	c_o^* =5435 m/s Material = steel

Table 4.6. Analysis of the simulated far resonance *component.*

We can summarize a preliminary comparison of approaches a) and b) relating to ideal conditions using simulated data thus:

- approach a) allows the extraction of a larger number of features, leading to a greater number of target parameters to estimate, compared with approach b);

- for resonance features (and related parameters) that can be extracted (estimated) by both techniques, resonance fitting and parameter estimation achieve comparable results in terms of accuracy (some results are only slightly more accurate when derived from approach a));

- approach a), thanks to the estimated TF spectrum, also provides a useful guideline for distinguishing between true and spurious resonances, which makes parameter estimation more robust;

- in both cases, either the far or the pure resonance component analysis can be omitted, as they provide the same kinds of results and similar degree of accuracy. If far component energy level and length are sufficient for reliable and high-resolution analysis in the frequency domain, it is preferred to the pure resonance response, the estimation of which may be affected by inaccuracy introduced by the splitting procedure. With simulated data, pure resonance processing results are frequently slightly worse than those obtained from far-resonance analysis.

These arguments are valuable if relating to noise-free simulated data, generated according to the same scattering theory used for developing most of the parameter estimation formulas; hence they must be validated and tested on the basis of real data analysis in the following section.

4.2 Analysis of real scattering data

The scattering response measured from the selected real target is considered (see Fig. 4.18). The incident pulse has been shown in Fig. 4.4. Results provided by applying approaches a) and b) are compared with those from simulated data presented in Section 4.1.
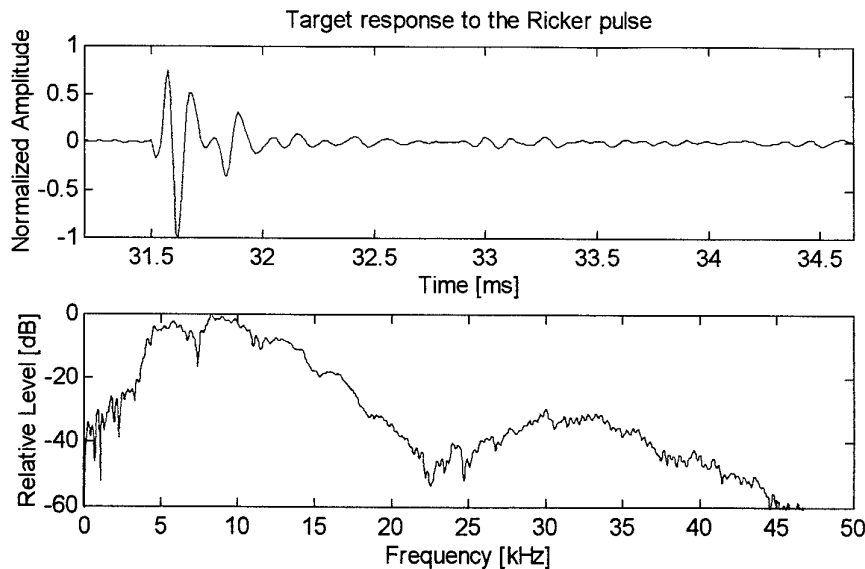
Fig. 4.18. Real target scattering response (time and frequency domains).

Real scattering data are mainly used for:

1. validating the selected RST-based acoustic scattering model, which simplifies the real scattering system;

2. validating the expectations about the generation of certain resonance wave families (e.g., Lamb-type and Scholte-Stoneley waves) and phenomena (e.g., strong-bending domain), which strongly depends on the scatterer geometry and physical properties;

3. testing the capabilities and evaluating the accuracy of AR models in estimating the system TF spectrum and extracting the selected resonance features in the presence of noise;

4. testing and comparing the capabilities of approaches a) and b), in terms of the number of target parameters to estimate, estimation accuracy and robustness to noise.

From Fig. 4.18 (see the spectrum plot) it is clear that the main component of the target response displays maximum energy at 8 kHz (response to the secondary frequency transmitted pulse); another significant, although noisier, component located at higher frequencies is the response to a contribution of the primary pulse. Both components will be considered in the processing phase.

4.2.1 Analysis of deconvolved global response

Fitting between the expected and estimated TF spectra is shown in Figs. 4.19 and 4.21. Resonance matching is in Figs. 4.20 and 4.22.

Matching between deconvolved global response (blue) and simulated TF (red) at low frequencies
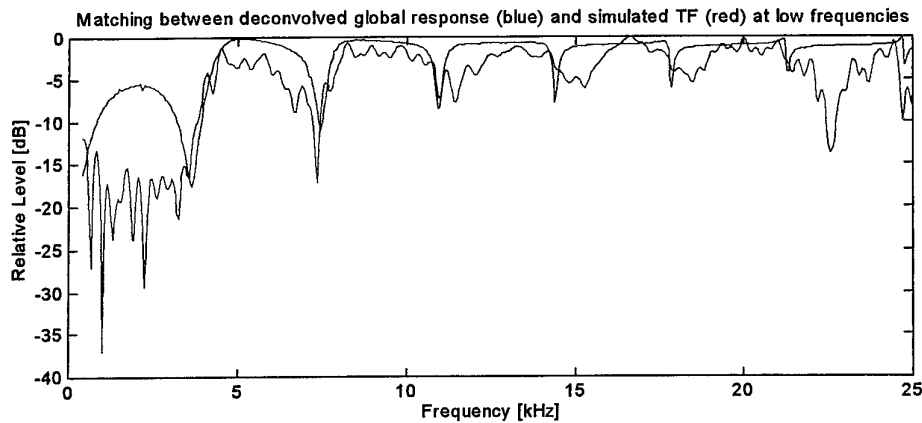
Fig. 4.19. Simulated and estimated TF spectra in the low-frequency domain.

Matching between extracted (red) and expected (green) S0 Lamb-type wave resonances (low frequencies)
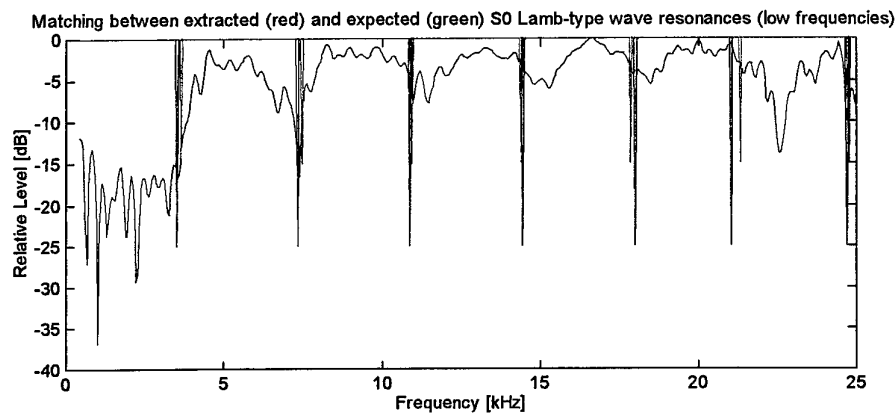

Fig. 4.20. Deconvolved response in the low-frequency domain, estimated and expected S_0 Lamb-type wave resonances (AR model order p=110).

Matching between deconvolved global response (blue) and simulated TF (red) at intermediate frequencies
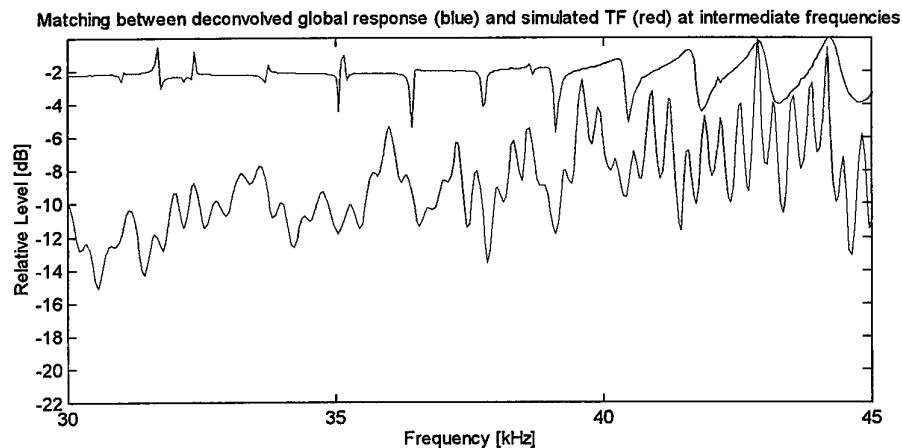

Fig. 4.21. TF spectrum, matched with the ideal one.

Matching between extracted (red) and expected (green) Scholte-Stoneley wave resonances at intermediate frequencies
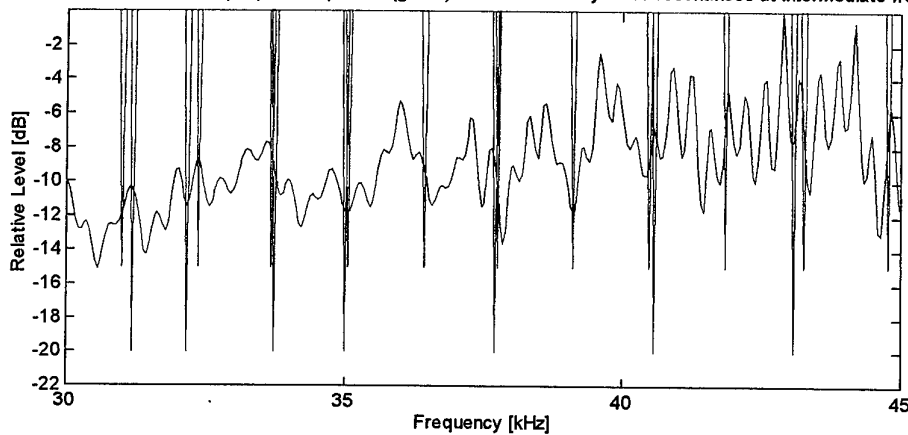

Fig. 4.22. Estimated TF at higher frequencies, extracted and expected Scholte-Stoneley wave resonances.

Feature	Parameter estimate	Parameter true value
Scholte-Stoneley waves Δf_A=1.3271 kHz	*outer radius* $\hat{a}$=25.36 cm	a_o=25 cm
Coincidence frequency f^{me} = 45.459 kHz	*relative thickness* $\hat{d}$=5.3 mm (with low confidence)	$d_o = a_o - b_o$=6 mm
S_0 Lamb-type waves Δf_{S0}=3.4713 kHz	shell material speed with a_o: $\hat{c}*$= 5452.7 m/s with $\hat{a}$: $\hat{c}*$=5531.2 m/s *Shell material* estimate is steel, with low confidence	c_o^*=5435 m/s Material = steel

Table 4.7. Summary of the estimation results from the deconvolved global response.

Model-data fitting in terms of TF spectrum is good in the frequency range [4,25] kHz, where most of the first spectral lobes are well defined. In addition, around 45 kHz the shape (although not the relative level) of the strong-bending region is approximately recovered, which is an important result for feature extraction purposes.

The spectral first lobe of the modeled TF spectrum is not recovered, hence the localization of its maximum is not feasible. Data-model mismatching for f<4 kHz is possibly a consequence of the limited adequacy of the used simulator in modeling the real case study. According to the considerations presented in [3], discrepancies between the RST-based model and real scattering data can occur in this frequency range.

In the range $f\in[4,25]$ kHz, where S_0 Lamb-type waves are examined (see Fig. 4.20), resonance fitting is accurate, hence the shell material estimate can be considered reliable. At intermediate frequencies, only some Scholte-Stoneley wave resonances fit well the simulated-TF corresponding resonances, as shown in Fig. 4.22.

The detection of the strong bending leads to a rough thickness estimation, as presented in Table 4.7. This result, derived from the localization of energy-enhancement and hence, at least roughly, of the coincidence frequency, is achieved because matching with the ideal TF spectral shape confirms a good fit with the strong-bending region. Under uncontrolled experimental conditions, one might interpret this energy enhancement as the deconvolution side effect of noise-level enhancement, and, hence, disregard it. For this reason, the thickness estimate is included in Table 4.7 with a low confidence level.

Even a small error in estimating the outer radius causes low-confidence in the shell material classification. Hence, the used relation is shown to be very sensitive to small changes of outer radius (and resonance localization) estimate, which is a significant limitation of this method.

Scholte-Stoneley resonance localization and matching with expected ones lead to the estimation of the related phase-speed dispersion curve, plotted and fitted with the simulated curve (from Fig. 2.5) in Fig. 4.23. Curve fitting is good in a wide range. Too few and sparse Scholte-Stoneley wave resonances are detected and matched correctly for providing their group dispersion curve. S_0 Lamb-type dispersion curves are presented in Figs. 4.24 and 4.25 in terms of group and phase speeds respectively.

Dispersion curves are compared with corresponding patterns derived from the analysis of the modeled TF (see Figs. 2.5 and 2.6). They are computed on the basis of the true outer radius value a_o.

Matching between estimated (red) and expected (blue) phase dispersion curves of A waves
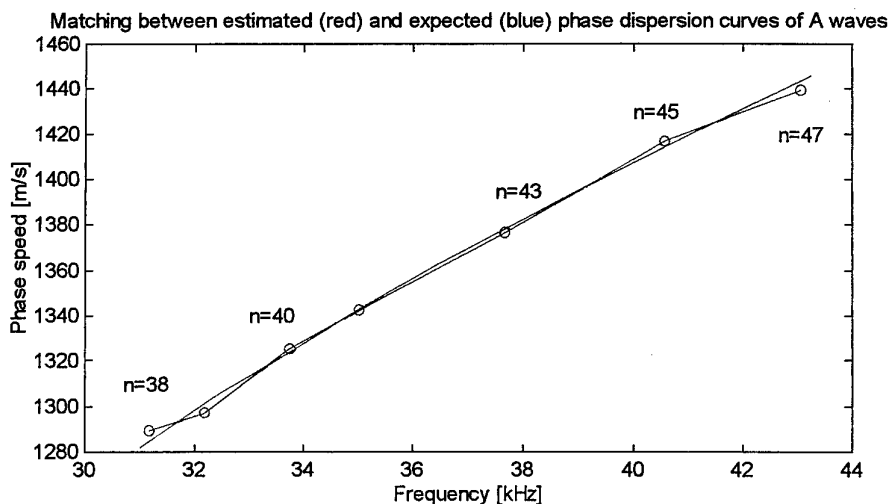
4.23. Matching of the phase dispersion curve related to the Scholte-Stoneley wave resonances.

Estimated (blue) and expected (red) group dispersion curves of S0 waves (mode order is included)
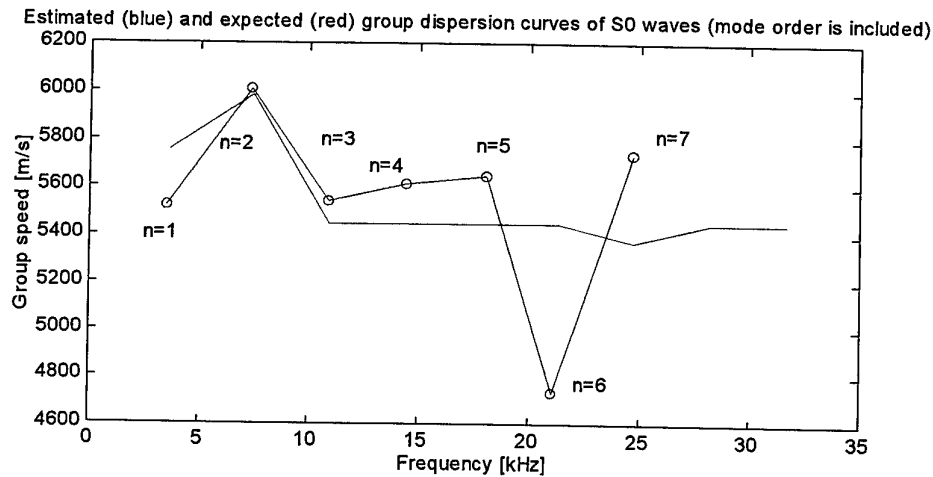
Fig. 4.24. Matching of S_0 Lamb-type group dispersion curve.

Estimated (blue) and expected (red) phase dispersion curves of S0 waves (mode order is included)
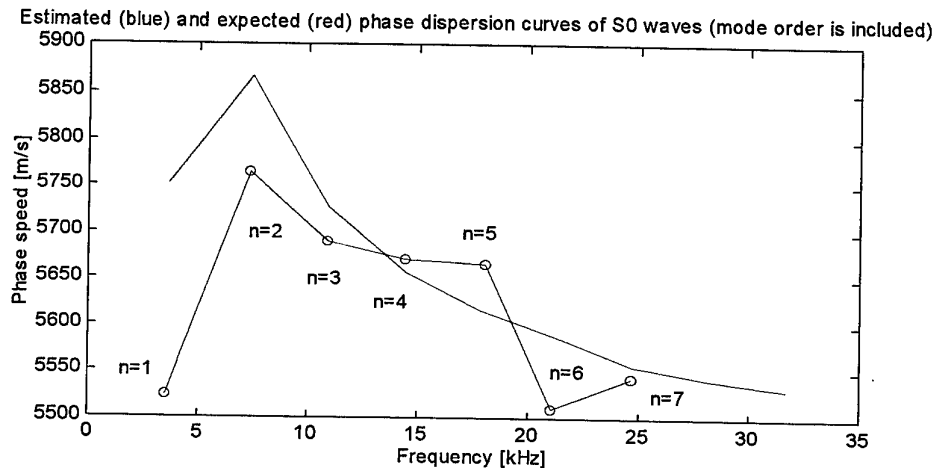
Fig. 4.25. Matching of S_0 Lamb-type phase dispersion curve.

Results obtained under real conditions degrade much with respect to simulated data processing:

1. The estimated TF spectrum is characterized by fluctuations and additional dips/peaks which may derive from scattering phenomena disregarded by the RST-based model. These unexpected phenomena increase the TF complexity and make the interpretation and the resonance detection and identification more difficult and less reliable.

2. Curve fitting at intermediate frequencies is poor. In this range the outer radius can be evaluated on the basis of a limited number of reliable measurements.

3. At low frequencies (f<4 kHz) the estimated TF spectrum does not meet with the expectation, because of partial model inadequacy.

Nevertheless, the strong-bending domain and the two families of peripheral waves the generation of which was expected by theory were recognized, and a number of resonances were extracted with a certain accuracy. This preliminary result implies that resonance analysis is feasible and can contribute to target characterization.

The numerical characteristics related to these features provide good parameter estimates. They are comparable with those obtained from simulated data in terms of accuracy, but processing is less robust, as only a limited number of resonance frequencies are localized, identified, and available for parameter estimation.

Resonance identification and localization can be only partially supported by data-model TF-curve fitting. Even when extracted resonance frequencies correspond well to those which are expected (see for example the resonances at f=10.866, 14.439 and 24.696 kHz pointed out in Fig. 4.20), fluctuations of the estimated TF spectral curve conceal corresponding expected dips and confirm the resonance extraction procedure.

4.2.2 Analysis of the deconvolved pure resonance component

TF spectral fitting for the deconvolved pure resonance component is generally poor, especially for f>20 kHz (Fig. 4.26). The resonance component isolation cannot show the expected resonances as evident peaks, because those amplitude fluctuations which characterize the global spectrum are even stronger, complicating the resonance spectrum and concealing the resonance peaks.

Nevertheless, resonance frequency fitting is good and allows reliable and accurate parameter estimation (Fig. 4.27 and Table 4.8). Even if many unexpected peaks make the response complicated, most of the identified S_0 Lamb-type resonances correspond to spectral peaks, as expected. Only a few Scholte-Stoneley wave resonances are detected and identified, but are sufficiently well localized to provide a good radius estimate.
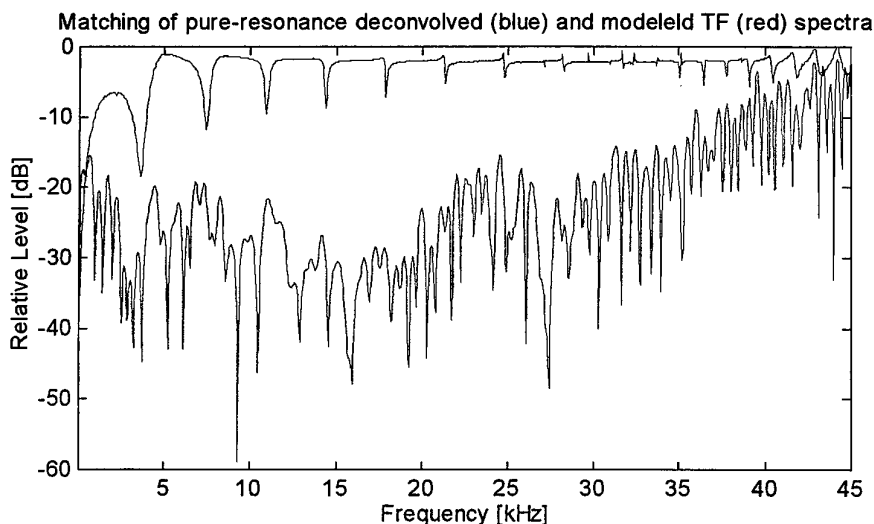
Fig. 4.26. Deconvolved pure-resonance TF spectrum, matched with the ideal model.

(a)

(b)
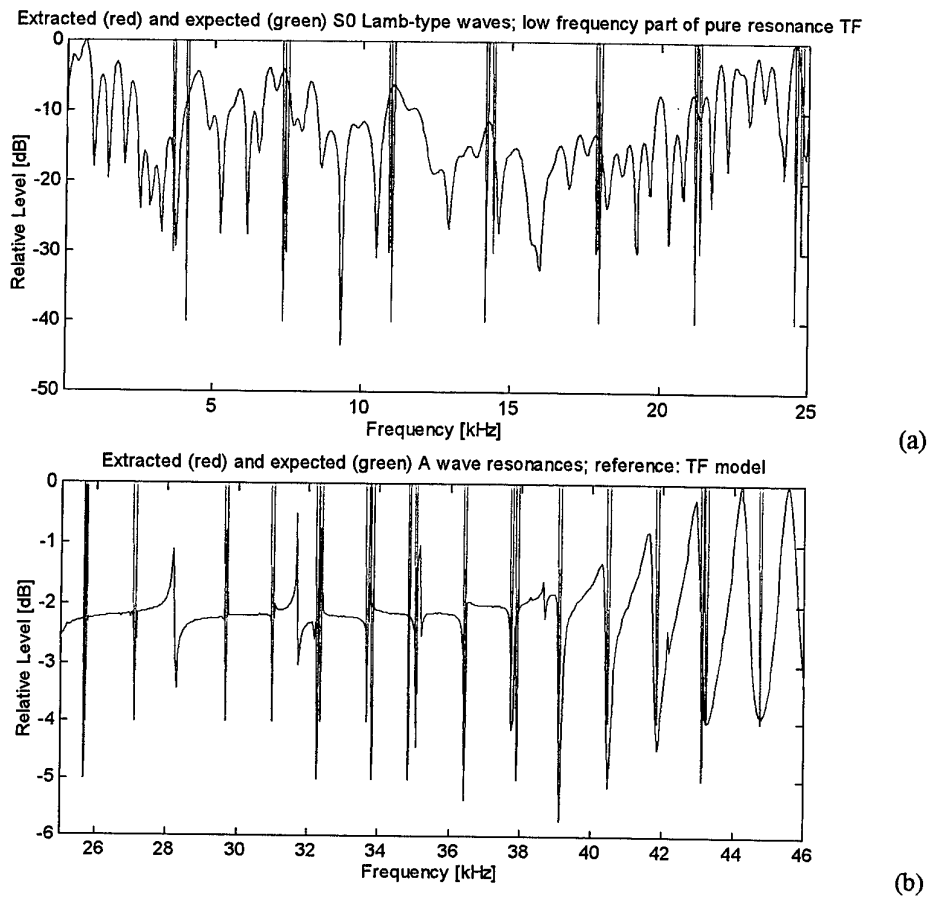
Fig. 4.27. Deconvolved pure-resonance *component; resonance identification (p=115). Low frequencies (a): S_0 Lamb-type wave fitting; high frequencies (b): Scholte-Stoneley wave fitting.*

Feature	Parameter estimate	Parameter true value
Scholte-Stoneley waves Δf_A =1.3554 kHz	*outer radius* $\hat{a}$ =24.83 cm	a^o =25 cm
S_0 Lamb-type waves Δf_{S0} =3.4842 kHz	shell material speed with a^o : $\hat{c}$ *=5473 m/s with $\hat{a}$: $\hat{c}$ *=5435.7 m/s *shell material* estimate: steel	c_o^* =5435 m/s Material = steel

Table 4.8. Analysis of the deconvolved pure resonance component of the response.

The present analysis confirms the performance decay of real data processing with respect to simulated data processing and the partial model-data mismatching, which have been outlined in the previous paragraph.

4.2.3 Analysis of the deconvolved far resonance component

Extracting the far resonance component from real data may not be feasible when the recorded output signal consists of a limited number of samples and scattered energy decreases rapidly after the end of the specular echo. This section addresses the feasibility and advantages of far-resonance processing when the SNR level is appreciable but the data length is limited. Time gating for isolating the far-resonance response is applied at 32.38 ms (see Fig. 4.18 above).

With reference to TF-pattern matching in Fig. 4.28, this component allows one to point out the peaks related to the S_0 Lamb-type wave resonances somewhat better than the pure-resonance response (compare Fig. 4.28 with Fig. 4.26). S_0 Lamb-type resonance matching is shown in Fig. 4.29. Even at higher frequencies ($f > 25$ kHz) the estimated TF spectrum is characterized by peaks roughly corresponding to the Scholte-Stoneley wave resonances (see Fig. 4.30). Only few resonances are detected and fitted well (hence the low-confidence level of the radius computation), but allow good estimates, as summarized in Table 4.9.
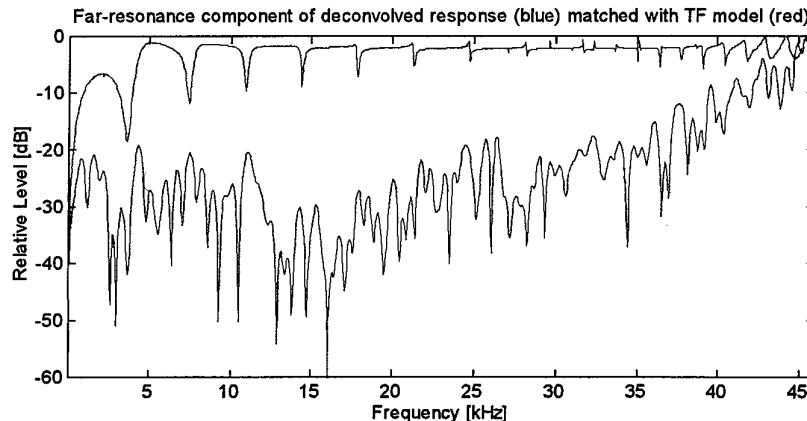

Fig. 4.28. Deconvolved far-resonance spectrum fitted with the TF model. Some resonances can be seen as peaks, as required.
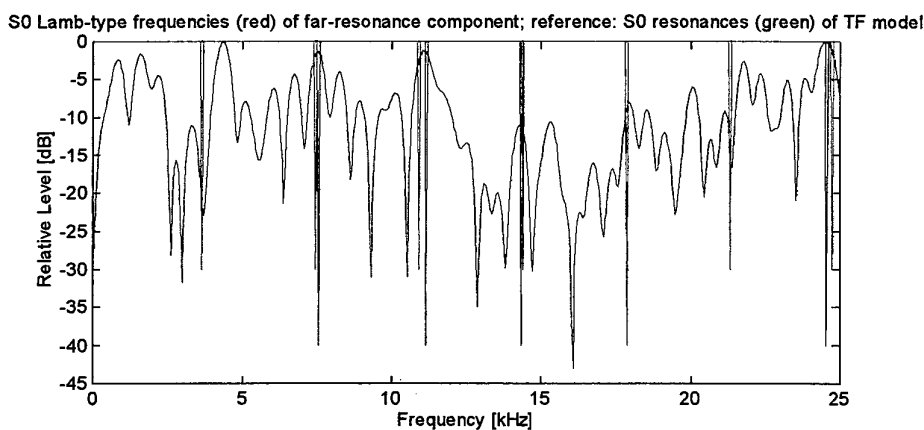

Fig. 4.29. Estimated and expected S_0 Lamb-type wave resonances (AR order p=100), referred to the estimated TF (blue).
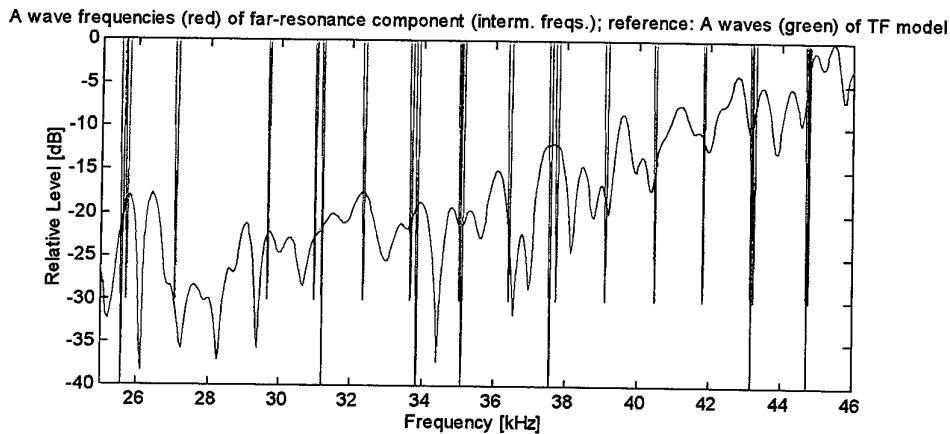
A wave frequencies (red) of far-resonance component (interm. freqs.); reference: A waves (green) of TF model

Fig. 4.30. Estimated Scholte-Stoneley wave resonances, matched with expected ones and referred to the estimated TF (blue).

Feature	Parameter estimate	Parameter true value
Scholte-Stoneley waves Δf_A=1.3393 kHz	*outer radius* $\hat{a}$=25.13 cm (low confidence level)	a^o=25 cm
S_0 Lamb-type waves Δf_{S0}=3.4531 kHz	shell material speed with a^o: $\hat{c}*$=5424 m/s with $\hat{a}$: $\hat{c}*$=5452 m/s *shell material* estimate is steel	c_o^*=5435 m/s Material = steel

Table 4.9. Analysis of the far resonance *component of the real scattering response.*

The evaluation of analyses of approach a) on real global, pure and far resonance components allows the following conclusions to be drawn:

- In this case, resonance response isolation can be considered redundant, as good model-data fitting and parameter estimation results have been obtained by processing the global response only. Decomposition is fundamental when global response analysis results are inadequate for resonance feature extraction, matching and processing.

- If the pure and far resonance responses are compared, as concerns fitting between spectral shape and expected resonance peaks, the far resonance component provides better results, in spite of the limited number of data samples and their lower energy. In terms of parameter estimation accuracy and reliability, processing outputs are comparable. Hence the analysis of the pure resonance component can be avoided here. It is more affected by possible inaccuracy of the employed algorithm of data decomposition in the case of real data.

In conclusion, the global and far resonance responses have provided the best results.

By comparing the results of approach a) applied to modeled and real data, it is clear that performances degrade in the real case more in terms of TF spectral data fitting and estimate confidence level than in terms of estimation accuracy.

Although the TF model-data matching is imperfect, AR-based analysis has achieved the detection and fitting of many foreseen resonances, and the employed model can be considered a valuable reference in a wide frequency range (around [4,46] kHz). Data-model fitting is poor in terms of both TF pattern and resonance detection and interpretation for $f<4$ kHz, which confirms what was deduced in [3].

As is well known, the selection of the bandwidth for preliminary deconvolution is noise-sensitive, and hence is a significant parameter influencing the performances of approach a). In this case study, in which data SNR level is generally good in the examined range, results have not been affected by noise enhancement.

4.2.4 Scattering analysis without preliminary deconvolution

On simulated data, approach a) has provided more complete and more accurate results than b). Present tests on real data aim to compare these methods under more critical conditions of geometry and data length.

A brief summary of the results obtained from the global, pure and far resonance real responses by means of approach b) is provided in Table 4.10. The confidence levels associated with the estimates are evaluated on the basis of the number of identified resonances used for parameter estimation and the accuracy of their frequency localization.

Response component	Outer radius $\hat{a}$ [cm]	Confidence Level	Shell material speed $\hat{c}^*$ [m/s]	Confidence Level
Global	25.04	Medium	5467 (if a_o is used) 5476 (if $\hat{a}$ is used)	Medium
Pure resonance	24.92	Medium	5422 (if a_o is used) 5405 (if $\hat{a}$ is used)	Medium
Far resonance	25.12	High	Not feasible	/

Table 4.10. Summary of parameter estimation results obtained from real scattering response processed by means of approach b).

Fewer results were obtained from the global response than those from the same scattered data processed by approach a) due to the limitations inherent in the processing method. The global response also provides slightly more accurate radius estimate than the other components.

By processing the far-resonance response, only the Scholte-Stoneley wave resonances are extracted, identified and localized with accuracy and high confidence level, providing good outer radius estimate; at low frequencies resonance fitting is so poor and unreliable that shell material estimation is omitted.

Comparison of the approaches a) and b) on real data lead to the following results.

- The performances of the preliminary deconvolution included in approach a) depend on the selection of the best frequency range to analyze, beyond which noise effects may increase dramatically. If correctly applied, it can provide a fundamental reference for matching extracted resonance features, even when the extraction of features linked to TF spectral shape is not feasible due to model inadequacy and data complexity.
  AR-based implicit deconvolution performed in approach b) is controlled by selecting the system model parameters by means of optimization procedures, but no parameter is included for selecting the frequency range to examine, as occurs if approach a) is chosen.

- Method b) allows us to emphasize the eventual inaccuracy of the decomposition algorithm in separating resonance from background components. This capability, not evident in approach a), can be useful for possible corrections of the splitting result.

- By following approach a) the analysis of the pure resonance part could be omitted as useless, while approach b) applied to the same data is complete and sufficiently reliable. Far resonance analysis by approach b) is limited to the evaluation of the outer radius, but provides very accurate and robust results.

- The model-based estimation results obtained from real data by applying the methods a) and b) allow us to conclude that although mostly based on RST, the used matching models between features and target parameters are quite robust in the case of real working conditions, given the target shape and approximately normal wave incidence.

In conclusion, approach a) is generally preferred in terms of number of parameters extracted and estimation reliability, while it is comparable with method b) in terms of estimation accuracy.

4.3 Discussion

A summary of the main considerations and of the most significant results follows.

4.3.1 The analysis of simulated data

Simulated data analysis is included in order to validate the feasibility and accuracy of the selected approaches under ideal conditions of absence of noise and perfect agreement between scattering target model and scattered data.

From either global, pure or far resonance components, analyzed by means of approaches a) and b), extraction and localization of the resonances of interest are accurate and lead to good estimates (being comparable in terms of accuracy) of a set of target parameters.

Those features linked with the *TF spectral shape*, which is strongly influenced by the response background, can be extracted and processed only by using *approach a) on the global response*. Hence, these processing results are the most complete in terms of obtained number of parameters, as they also provide thickness estimation.

Pure and far resonance responses processed by either approach a) or b) show how resonances can be emphasized by removing from scattered data the background, non-resonant component. Hence *parameter estimates* are generally more accurate than that obtained from the global response.

Under the ideal conditions of noise-free, long data sequences, *the far resonance component analysis may be preferred* if a detailed analysis of the intermediate frequency range is addressed, as the selection of this component is not affected by the eventual inaccuracy of splitting the global response into specular and pure resonance parts [7]. Nevertheless, in the far component analysis, the low-frequency resonance extraction can be imprecise, and some of the lowest resonances undetectable.

The first S_0 Lamb-type wave resonance frequency is always estimated inaccurately and frequently not detected. This inefficiency is reasonable, as it corresponds to a wide dip on the TF spectrum. Whenever Lamb-type resonances of higher orders are detected and identified well, the inaccurate or missed estimate of this dip does not influence subsequent estimation results.

Simulated data analysis is fundamental to the *definition of lower and upper boundaries of the examined frequency range*. The necessary condition for estimating most of the focused parameters with the proposed methods is to analyze the scattered spectrum at least in the range [2,46] kHz (i.e., $ka \in [2.0655, 47.5060]$), given the selected geometry and geophysical conditions.

4.3.2 Real data analysis

The fundamental result derived from the analysis of experimental scattered data consists of:

- confirming that, in addition to a strong specular reflection, an evident resonance component is generated;

- evaluating that the energy level and the time duration of the resonance component are sufficient for high-resolution resonance analysis in the frequency domain.

The bandwidth of the input Ricker pulse influences strongly the *frequency range in which processing is feasible* even after deconvolution, as under the assumption of linear acoustics, all of the energy scattered from the target belongs to a frequency range corresponding to the bandwidth of the incident pulse. As output data include part of the response to the primary emitted pulse, the analysis of intermediate frequencies is feasible, although not always reliable because of the lower SNR level by which it is characterized.

Inside the selected bandwidth, the *spectral shape* of the incident signal, being broadband and smooth, cannot influence in a significant way the AR-based resonance extraction process, even where SNR level is low.

4.3.3 Comparison between simulated and real data analysis

The analyzed real response cannot perfectly fit the selected RST-based model, as not all the constraints imposed by RST are satisfied [3] (see Chapter 1).

Nevertheless, some main concepts suggested by RST are validated on experimental data. As expected from theory,

- the isolation of the resonance component is feasible, although not always accurate, and generally allows a significant resonance analysis;

- by AR-based processing the resonances generated by scattering are shown to correspond to those TF poles having approximately unitary modulus in the z plane;

- the generation of the main families of peripheral waves (e.g., S_0 Lamb-type and Scholte-Stoneley waves) and of scattering phenomena, such as the strong-bending domain, is confirmed, and their properties (in particular, frequency location and consequent phase and group speed dispersion curves) are verified with a good degree of confidence.

Hence, the analysis results from RST-based simulated data provide a fundamental guideline for real-data processing.

If data-model matching in terms of TF spectra and resonance behavior is considered in detail, the following observations apply.

- The good fit between the estimated and expected S_0 Lamb-type resonance locations, which strongly depend on the aspect angle [2], allows one to estimate as normal the incidence, as forecast by the trial assessment [3].

- Major mismatching in terms of TF spectral shape is demonstrated by the lack of the first lobe at low frequencies, and in the presence of many unexpected (and not yet interpreted) peaks and dips covering the examined frequency domain.

- The proposed outer-radius estimation method may not be feasible (or at least non-robust) when either the strong-bending region is outside the analyzed frequency range, or other scattering phenomena conceal it. If scattered data were acquired while the sonar system moves around the target, other methods could be developed for providing target shape recovery and outer radius estimation.

- The proposed method for thickness estimation based on the localization of the first lobe maximum [2] is not feasible for scattering by finite-length cylindrical targets. In addition, both the selected methods for thickness estimation are noise-sensitive and can be used only for very thin walled ($h<\sim0.12$) air-filled or empty shells. Further investigations are needed to overcome this methodological limitation.

The approach a), consisting of deconvolution followed by AR-based modeling and analysis, is preferred to the proposed alternative method, as the former allows the extraction of significant features from the spectral shape, if applied to the global output response. In the deconvolution phase, particular attention should be paid to the selection of the most appropriate frequency range in which to operate, in order to limit eventual side effects of noise enhancement.

The isolation of the resonance component from real data does not show the generated resonance spectral peaks as well as from simulated data. Nevertheless, whenever time data sequences are long enough and present high SNR level, the far-resonance component analysis is useful and is preferred to the pure-resonance processing for extracting features (and, consequently, estimating target parameters) with good accuracy and an acceptable confidence level. In this case, the pure resonance part, adding neither further nor more refined knowledge on the scattering system, can be used for confirming obtained results, or omitted.

In conclusion, for processing the presented real data, the suggested analysis procedure consists in applying method a) to both the global and the far responses, and combining the related results.

5

Conclusions and future research

Some conclusions are sketched about the proposed approaches of data representation in the frequency domain, resonance scattering modeling, and signal processing for target characterization and classification.

5.1 Proposed methods of feature selection and analysis

The main purpose of the present work consisted of verifying whether resonance analysis is applicable to target characterization and classification.

On the basis of analysis of experimental data fitted with a selected scattering target model directly from Resonance Scattering Theory, this report has shown that this kind of approach is not only feasible, but can provide accurate and reliable results of target parameter estimation. The fundamental result obtained follows:

- The generation of resonance phenomena and, in particular, of some wave families, forecast by the Resonance Scattering Theory under ideal conditions, have been verified on real data, although the selected scattering model have not fitted perfectly with the real responses in the examined frequency range;

- the energy contribution of the generated resonance component from real scattered data has shown to be significant and has made resonance detection and identification feasible and reliable in most cases.

These observations justify the employment of these methods for extracting resonance frequencies from scattered responses (see the next section), and the development of analytical relations matching the extracted resonance features with target parameters of interest. Most of these analytical relations come from RST basic concepts and have been shown to provide good estimation results.

By starting from these fundamental considerations, several significant aspects of the proposed work are outlined in the following with more detail.

Although the RST-based target model is built on some unrealistic assumptions, model-data matching in the frequency domain has been considered acceptable in the frequency range [4,46] kHz, and has allowed us to obtain good parameter estimation results. Consequently, the analysis of simulated data has proven advantageous in predicting resonance behavior and providing a guideline for real data processing.

A separate analysis of the global, pure resonance and far resonance components [5] has been suggested. Results on experimental data have shown that performing the analysis of both global and far resonance responses can be the best solution in order to:

1) confirm the presence and accurately isolate some of the most evident resonance families, in particular the 0-order symmetric Lamb-type and the Scholte-Stoneley wave resonances; hence,

2) make the characterization robust and accurate, and

3) simplify resonance analysis.

Partial results coming from processing global and resonance responses separately can be fused according to some probabilistic/multi-hypothesis approach in order to further improve estimation robustness.

The resonance component has proven the most critical to isolate. For this reason its analysis has sometimes led to unreliable conclusions. On the other hand, the far-resonance component, whose energy is lower the further from the specular echo, is significant only when the acquired time data series is long enough and SNR level is high enough for providing reliable high-resolution frequency analysis.

5.2 The parametric approach to data representation

Basically two processing approaches have been selected and proposed:

a) the first consists in a preliminary deconvolution followed by an AR-based modeling step applied to the scatterer estimated impulse response;

b) the second method is based on the direct application of an AR model to scattered data, assuming an exciting signal which is a replica of the incident wave form.

Both are addressed to represent data in such a way that a large set of significant features useful for target classification can be extracted easily and accurately; in particular, they aim to detect, select and localize all the resonances generated by the target during the scattering phenomenon. Both approaches are shown to satisfy these requirements and, hence, to be adequate for the addressed purpose; nevertheless they present some peculiarities and differences.

The first approach has the significant advantage of providing also the scattering TF recovery, from which significant features can be extracted; hence it is more complete. In addition it can generally provide better results in terms of robustness of AR-based resonance extraction: the recovered TF is used also as a guideline for selecting the most reliable resonance frequencies, which correspond to TF spectral dips or peaks. As a consequence, the first procedure is preferred.

Although the TF of a scattering system should be represented by an ARMA model, the AR-based approach can be sufficient for the extraction of the main resonances of the

scattering field. This is a significant basis for the application of methods of parameter estimation [22]. ARMA modeling may be taken into account as an extension of the present work, since including zeros into the parametric model can lead to some advantages:

1. from RST, the zeros of the global TF should correspond to spectral dips, part of which can be associated to creeping wave frequencies [20];

2. a zero-pole model should allow one to reconstruct accurately the response spectral shape, and, hence, estimate the resonance damping factors and widths, which are linked by theoretical models [22] with other parameters of the scatterer, such as its material density.

Spectral representation is limited to an AR-based approach at the present, because, when signals are complicated and/or noisy, it is generally hard to optimize the orders p and q of an ARMA model, and, hence, find reliable results.

Finally, it is worthwhile to notice that in low/intermediate ka ranges only a few kinds of resonances are generated when the target shell is thin-walled and air-filled. This limits the number of coefficients needed for describing the system as a ratio of polynomials, and the number of parameters one can estimate. Nevertheless, this has allowed simple, and hence generally accurate, feature extraction. Actually, distinguishing among many estimated TF poles the significant wave resonances and grouping them into families can be a difficult task. The ka range around [2,46], selected as the minimum domain to analyze for estimating the selected target parameters in this case, is considered adequate for AR-based data representation, as the number of extracted resonances (spurious and not) has never overcome 50 and is thus a manageable number. Limiting the analyisis to this ka range is adequate for the studied target and trial configuration, but the domain of interest generally varies with the geophysical parameters of the inner and outer media, and with the shell material and aspect.

5.3 Future research

The considerations of the previous paragraphs, referred to the simple case study of acoustic scattering by an air-filled thin walled shell at broadside, can lead to the conclusion that the research in the field of acoustic resonance scattering can be further investigated for the purposes of target characterization and classification, and extended to more complicated real cases.

Next activities plan the relaxation of some of the imposed constraints; they concern three main phases:

1. extension of present RST-based investigations to *shells filled of other fluids* than air (in particular, the case of water inside); extension of resonance feature selection and processing related to those phenomena depending on inner fluid;

2. extension to resonance investigation on data scattered by targets excited *at aspect angles different from broadside*; focus on phenomena depending on the target aspect angle; in particular, analysis of data at other target aspects might allow the estimation

of target length, which is hard to achieve when data are scattered from broadside aspect;

3. study of resonance scattering by *solid cylinders, spheres, natural objects and irregular man-made objects* to compare with scattering behavior of cylindrical shells.

The extension to more general target classes and to more realistic operating conditions will allow these processing methods to be applied to the characterization and classification of mine-like objects and real mines by the generalization of the parameter estimation methods which at present need *a priori* knowledge of target shape, aspect and inner medium.

Each processing method developed will be validated and tested on simulated and real data.

Acknowledgments

Many thanks go to John Fawcett for his fundamental contribution to resonance scattering modeling.

References

[1] Flax L., Dragonette L.R., and Uberall H., Theory of elastic resonance excitation by sound scattering. *Journal of the Acoustical Society of America*, 63, 1978: 723-731.

[2] Veksler N.D., *Resonance acoustic spectroscopy*. Berlin Springer, 1993.

[3] Fox W.L.J., Fawcett J.A., Jourdain-Albonico D., and Tesei A., Measurements of free-field acoustic scattering from cylindrical shells, SACLANTCEN SM-331. La Spezia, Italy, SACLANT Undersea Research Center, 1997.

[4] Veksler N.D., Maze G., Ripoche J., and Porochovskii V., Scattering of an obliquely incident plane wave by a circular cylindrical shell. Results of computations. *Acustica - Acta Acustica*, 82, 1996: 689-697.

[5] de Billy M., Determination of the resonance spectrum of elastic bodies via the use of short pulses and Fourier Transform theory, *Journal of the Acoustical Society of America*, 79, 1986: 219-221.

[6] Weyker R.R., and Dudley D.G., Identification of resonances of an acoustically rigid sphere. *IEEE Journal of Oceanic Engineering*, 12, 1987: 317-326.

[7] Azimi-Sadjadi M.R., Wilbur J.E., and Dobeck G.J., Isolation of resonance in acoustic backscatter from elastic targets using adaptive estimation schemes. *IEEE Journal of Oceanic Engineering*, 20, 1995: 346-353.

[8] Wilbur J., and McDonald R.J., Resonant pole identification from the acoustic backscatter of small submerged multi-specular elastic targets. Piscataway, NY, *IEEE ICASSP '96*. 1996: 2785-2788.

[9] Breintenbach E.D., Uberall H., and Yoo K.-B., Resonant acoustic scattering from elastic cylindrical shells. *Journal of the Acoustical Society of America*, 74, 1983: 1267-1273.

[10] Murphy J.D., Breintenbach E.D., and Uberall H., Resonance scattering of acoustic waves from cylindrical shells. *Journal of the Acoustical Society of America*, 64, 1978: 677-683.

[11] Dragonette L.RDrumheller., D.M., Gaumond C.F., Hughes D.H., O'Connor B.T., Yen N.-C., and Yoder T.J., The application of two-dimensional signal transformations to the analysis and synthesis of structural excitations observed in acoustical scattering. *Proceedings of the IEEE*, 84, 1996: 1249-1263.

[12] Talmant M., Izbicki J.-L., Maze G., Quentin G., and Ripoche J., External wave resonances on thin cylindrical shells. *Journal Acoustique*, 4, 1991: 509-523.

[13] Magand F., and Chevret P., Time frequency analysis of energy distribution for circumferential waves on cylindrical elastic shells. *Acustica - Acta Acustica*, 82, 1996: 707-716.

[14] Bhattacharyya G.K., and Johnson R.A., *Statistical concepts and methods*, New York, Wiley, 1977.

[15] Sessarego J.-P., Sageloli J., Gazanhes C., and Uberall H., Two Scholte-Stoneley waves on doubly fluid-loaded plates and shells. *Journal of the Acoustical Society of America*, 101, 1997: 135-142.

[16] Sessarego J.P., Sageloli J., Degoul P., Flandrin P., and Zakharia M., Analyse temps-frequence de signaux en milieu dispersif - application a l'etude des ondes de Lamb. *Journal Acoustique*, 3, 1990: 273-280.

[17] Kay S.M., *Modern spectral estimation: theory and application*, New York, Prentice Hall, 1988.

[18] Ljung L., *System identification. Theory for the user*, New York, Prentice Hall, 1987.

[19] Soderstrom T., and Stoika P., *System identification*, London, Prentice Hall, 1989.

[20] Gaunaurd G.C., and Brill D., Acoustic spectrogram and complex-frequency poles of a resonantly excited elastic tube. *Journal of the Acoustical Society of America*, 75, 1984: 1680-1693.

[21] Bentech Subsea AS, *Simrad TOPAS PS 040 Operator Manual*.

[22] Batard H., Talmant M., and Quentin G.J., The Acoustical Characteristics Estimation Method (MECA) applied to cylinders and shells. *Acta Acustica*, 2, 1994: 333-342.

Annex A

Characteristic physical parameters of some common solid materials

NOTE: The parameter c^*, characteristic of each solid material, is provided as a combination of c_p and c_s by the formula: $c^* = c_s \sqrt{\dfrac{2}{1-\nu}}$,

where ν is the Poisson's ratio: $\nu = \dfrac{c_p^2 - 2c_s^2}{2(c_p^2 - c_s^2)}$

Solid	c_p [m/s]	c_s [m/s]	ρ [g/cm^3]	ν	c^* [m/s]
steel	5950	3240	7.7	0.2892	5435.0
aluminum	6420	3040	2.7	0.3555	5355.2
copper	4760	2325	8.93	0.3433	4057.6
gold	3240	1200	19.7	0.4205	2229.3
lead	2160	700	11.4	0.4413	1324.4
nickel	5480	2990	8.85	0.2881	5011.4
platinum	3260	1730	21.4	0.3040	2932.6
silver	3650	1610	10.4	0.3792	2889.8
zinc	4210	2440	7.1	0.2471	3976.8
glass	5640	3280	2.32	0.2445	5336.6
sandstone	2920	1840	2.2	0.1707	2857.5
fine sand	1742	382	1.98	0.4747	745.4
coarse sand	1836	250	2.03	0.4906	495.34
clay	1500	<100	1.5	if c_s=80:0.4986	159.77
basalt	5250	2500	2.7	0.3534	4396.7
fiber glass	2400(used)-2200	1283(used)-1176	1.8	0.3	2168.5
WAX	1450	110	1.5	0.4971	219.366

Annex B

Characteristic physical parameters of some fluids

fluid	c [m/s]	ρ [g/cm^3]
air	331	0.001
distilled water	1497	1
sea water	1521	1
chloroform	987	1.49

Security Classification	Project No.
NATO UNCLASSIFIED	031-2

Document Serial No.	Date of Issue	Total Pages
SR-265	October 1997	68 pp.

Author(s)

A. Tesei, W. Fox, A. Maguer, A. Løvik

Title

Resonance scattering analysis by autoregressive models applied to air-filled, cylindrical, thin walled shells in water.

Abstract

Autoregressive (AR) parametric spectral estimation of the scatterer transfer function is applied to the analysis of acoustic scattering by elastic objects.

In accordance with Resonance Scattering Theory (RST), the specular and resonance components of the scattering field are differentiated. AR models and consequent resonance analysis are applied to both the global scattering response and to the resonance component separately. The AR-based representation is useful for detecting and localizing resonances in the frequency domain. The capability of AR models to estimate resonance frequencies accurately is shown. Among the extracted poles of the AR model, a subset of resonance frequencies is selected and processed in order to characterize a scattering object in terms of geometrical and geophysical parameters on the basis of analytical matching relations, derived from the RST.

The targets considered are elastic, cylindrical, thin walled shells in water under free-field conditions. Analysis is performed on simulated and real data in the ka range (0,50].

Keywords

Free-field acoustic scattering – resonance analysis – AR-based spectral estimation

Initial Distribution for SR 265

Ministries of Defence		Scientific Committee of National Representatives	
DND Canada	10	SCNR Belgium	1
CHOD Denmark	8	SCNR Canada	1
DGA France	8	SCNR Denmark	1
MOD Germany	15	SCNR Germany	1
HNDGS Greece	12	SCNR Greece	1
MARISTAT Italy	9	SCNR Italy	1
MOD (Navy) Netherlands	12	SCNR Netherlands	2
NDRE Norway	10	SCNR Norway	1
MOD Portugal	5	SCNR Portugal	1
MDN Spain	2	SCNR Spain	1
TDKK and DNHO Turkey	5	SCNR Turkey	1
MOD UK	20	SCNR UK	1
ONR USA	42	SCNR USA	2
		French Delegate	1
		SECGEN Rep. SCNR	1
NATO Commands and Agencies		NAMILCOM Rep. SCNR	1
NAMILCOM	2		
SACLANT	3	**National Liaison Officers**	
CINCEASTLANT/			
COMNAVNORTHWEST	1	NLO Canada	1
CINCIBERLANT	1	NLO Denmark	1
CINCWESTLANT	1	NLO Germany	1
COMASWSTRIKFOR	1	NLO Italy	1
COMMAIREASTLANT	1	NLO Netherlands	1
COMSTRIKFLTANT	1	NLO Spain	1
COMSUBACLANT	1	NLO UK	1
SACLANTREPEUR	1	NLO USA	1
SACEUR	2		
CINCNORTHWEST	1		
CINCSOUTH	1		
COMEDCENT	1		
COMMARAIRMED	1		
COMNAVSOUTH	1	**Sub-total**	208
COMSTRIKFORSOUTH	1		
COMSUBMED	1	SACLANTCEN	30
NC3A	1		
PAT	1	**Total**	238